Pro Gradu

Annealing Study of Bismuth Thin Films

Mika Oksanen

June 23, 2010

UNIVERSITY OF JYVÄSKYLÄ
NANOSCIENCE CENTER
DEPARTMENT OF PHYSICS
NANOPHYSICS

Preface

The work reported in this Master's thesis has been done between June 2008 and June 2010 at Nanoscience Center at the Department of Physics in the University of Jyväskylä.

First, I would like to thank my supervisor Professor Ilari Maasilta, who has been an excellent advisor in both experimental and theoretical work as well as in the writing process of this Master's thesis. I would also like to than him for the interesting research topic and the opportunity to work in his nanophysics group. In addition, I would like to thank Drs. Jenni Karvonen and Panu Koppinen, and PhD. student Minna Nevala for their help and guidance in the experimental work. The working atmosphere in Nanoscience Center has been enjoyable, for which I would like to thank the whole staff.

Finally, I would like to thank my fiancée Salla for the endless love and support.

Jyväskylä June 23, 2010

Mika Oksanen

Abstract

Electrical and magnetotransport properties of thin bismuth films were studied in the range of 4.2 - 295 K in applied magnetic fields up to 3.5 T. The bismuth films were deposited on mica and SiO_x substrates and subjected to post deposition thermal annealing in order to improve the crystal structure. Annealed films showed lower resistivities and higher magnetoresistance as compared to the non annealed samples, however, the resistivity behavior was non-metallic and the mean grain size in the films were not significantly increased. A two carrier model for magnetoresistance and Hall coefficient was used to extract carrier mobilities and concentrations from the transport data.

Tiivistelmä

Työn nimen voisi suomentaa "Lämpökäsittelyn vaikutus vismutti-ohutkalvojen ominaisuuksiin". Työssä tutkittiin termisen anniilauksen vaikutusta tyhjiöhöyrystettyjen vismutti-ohutkalvojen kiderakenteeseen ja sähköisiin ominaisuuksiin.

Vismutti on puolimetalli, jolla on erittäin mielenkiintoisia ominaisuuksia. Sen vapaiden elektronien efektiivinen massa on pienimmillään vain tuhannesosa vapaan elektronin massasta, varauksenkuljettajien vapaa matka voi olla jopa millimetrin luokkaa alhaisissa lämpötiloissa, sen elektronitiheys on useita kertaluokkia pienempi kuin normaaleilla metalleilla, ja sillä on alhainen Fermienergia ~ 38 meV. Vismutti on eniten diamagneettinen materiaali, jonka vastus voi kasvaa useita miljoonia kertoja ulkoisessa magneettikentässä (magnetoresistanssi) alhaisissa lämpötiloissa. Magnetoresistanssin suuruus voi olla $\rho(B)/\rho_0 \approx 10^6$ 4.2 K lämpötilassa ja 10 T magneettikentässä. Tämä on huomattavasti suurempi efekti kuin nk. Suuri magnetoresistanssi (GMR) ja on verrattavissa Kolossaaliseen magnetoresistanssiin (CMR). Lisäksi vismutissa resistanssin riippuvuus magneettikentästä on ei-hystereettinen. Vismuttiohutkalvot voisivat olla hyvin käyttökelpoisia magneettisina antureina, mikäli suuri magnetoresistanssiefekti säilyy myös ohutkalvoissa. Tämä riippuu oleellisesti ohutkalvojen kidekoosta, koska pieni kidekoko pienentää voimakkaasti varauksenkuljettajien vapaata matkaa ja magnetoresistanssin suuruutta.

Tässä työssä raportoidaan termisen anniilauksen vaikutuksesta tyhjiöhöyrystettyjen ohutkalvojen sähköisiin ominaisuuksiin ja magnetoresistanssin suuruuteen. Terminen anniilaus tarkoittaa ohutkalvojen lämmittämistä hyvin lähelle sulamispistettä, ja niiden pitämistä tässä lämpötilassa useita tunteja, jolloin kiderakenne uudelleenjärjestyy ja kidekoon pitäisi kasvaa. Vismuttiohutkalvot deponoitiin oksidoiduille pii - sekä mica - substraateille. Näytteiden sähköiset ominaisuudet on määritetty resistiivisyys, magnetoresistanssi, ja Hall - mittauksilla 4.2 – 295 K lämpötiloissa sekä 3.5 T magneettikentässä. Tutkittujen ohukalvojen paksuus vaihteli 65 nm ja 1 µm välillä. Ohutkalvojen varauksenkuljettajien tiheydet ja mobiliteetit määritettiin käyttämällä klassista kahden varauksenkuljettajan mallia magnetoresistansille ja Hall - kertoimelle.

Tulosten pääasiallinen johtopäätös on, että annilauksen jälkeen magnetoresistanssin suuruus kasvaa kaikissa tutkituissa näytteissä, mutta resistiivisyys on ei-metallista eikä keskimääräinen kidekoko ohutkalvoissa kasva. Lisäksi mica - substraatille deponoiduissa näytteissä on suurempi magnetoresistanssi kuin piisubstraateille deponoiduissa.

Contents

Introduction

Bismuth is a semimetal element with unusual transport properties. Bismuth has a highly anisotropic Fermi surface, small anisotropic effective masses, low carrier densities, and long carrier mean free paths. Being a semimetal, bismuth has a small overlap between the electron conduction band and the hole valence band. Very low effective masses together with elongated Fermi surfaces of the carriers yield a Fermi wavelength of about 400 Å, as opposed with few Å in normal metals [1]. The carrier mean free paths can be of the order of millimeter at 4.2 K [2]. Due to these properties, quantum transport and quantum size effects have been studied extensively in bismuth.

Bismuth is the most diamagnetic of all materials. Bulk bismuth exhibits very large ordinary magnetoresistance (MR), because of the long relaxation time τ and large cyclotron frequency $\omega_c = eB/m^*$. The magnitude of the effect can be as high as $\rho(B)/\rho_0 \approx 10^6$ at 4.2 K and at field of 10 T. This is comparable to the Colossal magnetoresistance (CMR) [4], and much higher than the few hundred % of Giant magnetoresistance (GMR). Furthermore, compared to GMR and CMR, the field dependency of MR in bismuth is simple and non hysteretic up to very high fields. Bismuth thin films would thus be useful in wide range of magnetic field sensing applications, provided that the films are of high quality.

Besides magnetic applications, high quality bismuth films would have several other important uses. Thermoelectric materials convert temperature difference into electricity and vice versa. These materials can be used for power generation (Seebeck effect) or cooling (Peltier effect). Thermoelectric materials can cool or heat without moving parts or toxic gases. The efficiency of a thermoelectric material is defined by the figure of merit $ZT = (S^2\sigma/\kappa)T$, where S is thermoelectric power, σ is the electrical conductivity, κ is the thermal conductivity, and T is temperature. Bismuth has favorable properties to achieve large ZT, e.g. low thermal conductivity (8 W/mK) and large thermoelectric power (50 – 100 µV/K). In bulk bismuth however, the ZT is limited by the conduction and valence band overlap, causing bismuth to be a compensated semimetal, which means that contributions of electrons and holes to S cancel each other. It has been predicted, that lower dimensionality (2D or 1D) could enhance the thermoelectric efficiency of bismuth [10]. The thermoelectric properties of low dimensional bismuth samples have been measured, but the results have suffered form the polycrystal structure of the samples [3].

Bismuth is also used as a radiation absorber in superconducting transition edge sensors (TESs), which are being developed in our group [5]. TESs consist of a superconducting film operated at the transition temperature, and it thus has a very high sensitivity for a small heat signal (e.g. absorption of a single photon). Bismuth is a heavy material, capable of stopping radiation at a reasonably thin layer, and it thus has a low heat capacity which is favorable to the performance of the sensor. Furthermore, the electrical and thermal conductivity of the absorber affect the sensor performance, which depend on the film quality.

The aim of this thesis is to study the efficiency of thermal annealing to improve the crystal quality of bismuth thin films. Various methods for fabrication of bismuth thin films have been used in the literature, including molecular beam epitaxy (MBE), electrodeposition and vapor deposition. While MBE produces high quality epitaxial bismuth films, it is a slow and expensive technique. Electrodeposition and vapor deposition (sputtering, vacuum evaporation) can produce high quality films, if the samples are subjected to suitable thermal treatment. They are also suitable for large scale production. For the TESs, vacuum evaporation is currently used in devices fabricated at NSC.

Here we report the effect of thermal annealing on bismuth thin films deposited on muscovite mica and SiO_x substrates. Standard microfabrication techniques are used in sample fabrication. The efficiency of post deposition annealing has been proven for films with thickness over 1 µm, here we study the similar process applied for much thinner films (65 – 380 nm). The electrical properties of the thin films are characterized with resistivity measurements between 4.2 and 295 K, and with magnetotransport measurements at 4.2K in fields up to 3.5 T. A two carrier model for magnetoresistance and Hall coefficient is used to estimate carrier mobilities and concentrations of the samples.

Chapter 1

Theory

This chapter introduces the unique band structure of bulk bismuth. Semiclassical magnetotransport theory is explored and the magnetotransport properties of bismuth are explained in this context.

1.1 Bismuth band structure

Bismuth is a semimetal with A7 rhombohedral crystal structure and two atoms per unit cell. The Brillouin zone of bismuth is depicted in figure 1.1. Bismuth has one hole pocket and three electron pockets, which occupy only a few thousandth of the Brillouin zone. The electron pockets are not exactly ellipsoids, but are often approximated as such. They also have two of their principal axes slightly tilted from the crystal axes. The hole surface at T-point is a spheroid with the axis parallel to the trigonal axis. Due to the complicated band structure, most of the transport properties of bismuth are anisotropic. Bulk bismuth exhibit resistivity behavior i.e. resistivity increases with temperature.

The band structure of bismuth is illustrated in figure 1.2. The electron energy bands at L-point are highly non-parabolic, which is due to the strong coupling between these bands. The T-point valence band is roughly parabolic. Being a semimetal, bismuth has a small overlap between conduction and valence band, and a low Fermi energy $\mathrm{E}_F \sim 25$ meV.

The dispersion relation for the L-point carriers is given by the Lax model [8]

$$E_L(\mathbf{k}) = -\frac{E_g}{2} \pm \frac{E_g}{2}\sqrt{1 + \frac{2\hbar^2}{E_g}\left(\frac{k_x^2}{m_x} + \frac{k_y^2}{m_y} + \frac{k_z^2}{m_z}\right)}, \tag{1.1}$$

where E_g is the direct band gap at L-point. The - sign is for L-point holes and + sign for L-point electrons. The effective masses m_i in equation (1.1) have to be calculated from the effective mass tensor of bismuth. For the electron pocket at **A** in figure 1.1, the effective mass tensor can be written in the trigonal axis system [x,y,z] as

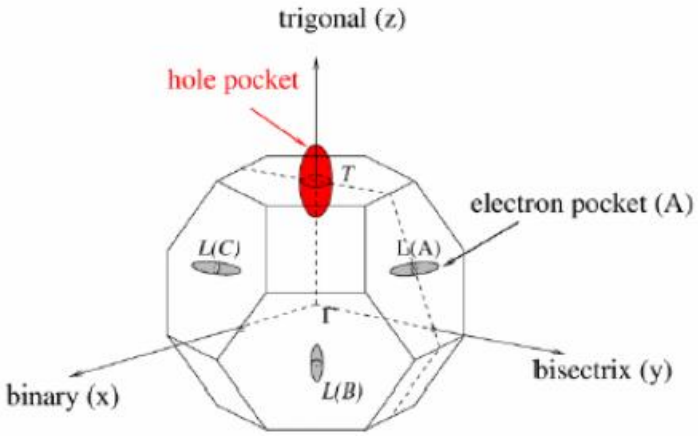

Figure 1.1: The Brillouin zone of bismuth, indicating the Fermi surface and the location of the hole pocket and three electron pockets [6].

$$\mathbf{M}_{e,\mathbf{A}} = \begin{pmatrix} m_{e1} & 0 & 0 \\ 0 & m_{e2} & m_{e4} \\ 0 & m_{e4} & m_{e3} \end{pmatrix}. \tag{1.2}$$

The elements in (1.2) at T = 0 K are $m_{e1} = 0.00118m_0$, $m_{e2} = 0.263m_0$, $m_{e3} = 0.00516m_0$, and $m_{e4} = 0.0274m_0$, where m_0 is the free electron mass. The high anisotropy of the ellipsoids is apparent (e.g. $m_{e2} \gg m_{e1}$) as well as the very small value of some of the mass components. The effective mass tensors of the other L-point pockets can be obtained by rotating (1.2) for 120° and 240° about the trigonal axis. The hole band is significantly simpler than the electron bands. Since the single hole pocket has its principal axis parallel with the trigonal axis of the Brillouin zone, the effective mass tensor is diagonal with the elements m_{h1}=$m_{h2} = 0.059m_0$, and $m_{h3} = 0.630m_0$. These values are taken to be temperature independent, whereas the electron effective masses vary significantly with temperature, given by the equation [11]

$$[\mathbf{m}_e(T)]_{\mathrm{ij}} = \frac{[\mathbf{m}_e(T)]_{\mathrm{ij}}}{1 - 2.94 \times 10^{-3}T + 5.56 \times 10^{-7}T^2}. \tag{1.3}$$

This gives a variation by a factor of 6 in the effective masses between 0 and 300 K. Similarly, the direct band gap at L-point varies with temperature, as well as the band overlap, which is roughly constant up to 80 K (-38 meV) and increases to -104 meV at 300 K. Various parameters of bulk bismuth are summarized in table 1.1.

1.1.1 Density of states

The density of states resulting from the peculiar band structure is worth exploring. The density of states for the parabolic valence band is considered first, the dispersion

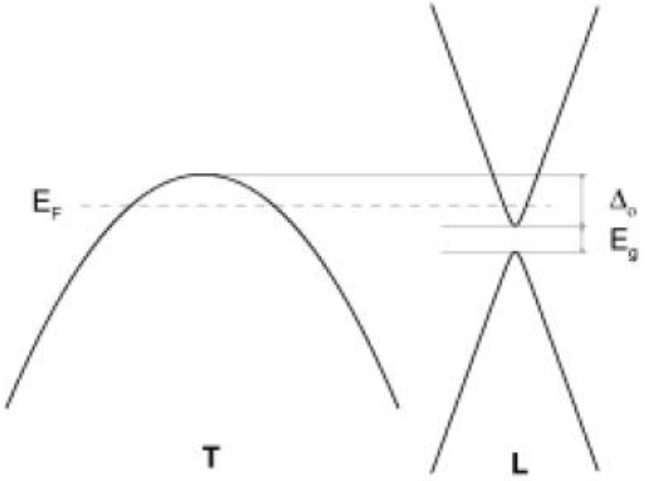

Figure 1.2: Schematic diagram of the Bi band structure at the L-points and T-point near Fermi level, showing the band overlap Δ_0 between the L-point conduction band and the T-point valence band. The L-point electrons are separated from the L-point holes by a small band gap E_{gL}. At T = 0 K, Δ_0 = -38 meV and E_{gL} = 13.6 meV [7].

Property	Symbol	Value
Mass density (g/cm^3)		9.8
Melting point (K)		544.4
Thermal conductivity (W/mK)	κ	7.87
Resistivity (μΩcm)	ρ	106.8
Electron Density (1/cm^3)(300K)	n	3.00×10^{18}
Electron Density (1/cm^3)(4.2K)	n	2.88×10^{17}
Hole density (1/cm^3)(4.2K)	p	3.00×10^{17}
L-point band gap (meV)	E_{gL}	13.6
Band overlap (meV)	Δ_0	-38
electron mobility at 77 K	μ_1	68.0
in units $\times10^4$ cm^2/Vs	μ_2	1.6
	μ_3	38.0
	μ_4	-4.3
Hole mobility at 77 K	$\mu_{h1} = \mu_{h2}$	12.0
in units $\times10^4$ cm^2/Vs	μ_{h3}	2.1

Table 1.1: Various parameters of bulk bismuth [9, 10, 32, 33].

relation of an ellipsoid being

$$E(\mathbf{k}) = \frac{\hbar^2 k_x^2}{2m_x} + \frac{\hbar^2 k_y^2}{2m_y} + \frac{\hbar^2 k_z^2}{2m_z}. \tag{1.4}$$

The volume of the ellipsoid in **k**-space is

$$V_k = \frac{4\pi}{3} k_x^E k_y^E k_z^E, \tag{1.5}$$

where

$$k_i^E = \frac{\sqrt{2m_i E}}{\hbar}. \tag{1.6}$$

Since the volume occupied by a one element in **k**-space is $(2\pi)^3/\mathrm{V}$, the total number of states

$$N(E) = 2 \times \frac{4\pi}{3} k_x^E k_y^E k_z^E \frac{V}{(2\pi)^3}, \tag{1.7}$$

where the factor 2 comes from spin degeneracy. By substituting (1.6) into (1.7) and eliminating k, one obtains

$$N(E) = \frac{2\sqrt{2}V}{3\pi^2\hbar^3} \left(m_x m_y m_z\right)^{1/2} E^{\frac{3}{2}}. \tag{1.8}$$

The three-dimensional density of states per unit volume is obtained by taking the derivative of (1.8) with respect to energy,

$$D(E) = \frac{1}{V}\frac{\mathrm{dN}}{\mathrm{dE}} = \frac{\sqrt{2}}{\pi^2\hbar^3} \left(m_x m_y m_z\right)^{1/2} E^{\frac{1}{2}}. \tag{1.9}$$

Thus the density of states for the hole band has the usual $\mathrm{D(E)} \propto \mathrm{E}^{1/2}$ dependency.

The density of states of the L-point conduction band can be derived using the Lax model (eq. (1.1)). The volume in **k**-space at energy E is still given by (1.5), but the wavevector k is now

$$k_i^E = \sqrt{\frac{2m_i}{\hbar^2}\left(\frac{E^2}{E_g} - E\right)} \tag{1.10}$$

The number of states can again be calculated using (1.7)

$$N(E) = 3 \times 2 \times \frac{4\pi}{3} k_x^E k_y^E k_z^E \frac{V}{(2\pi)^3} = \frac{2\sqrt{2}V}{\pi^2\hbar^3} (m_x m_y m_z)^{1/2} \left(\frac{E^2}{E_g} - E\right)^{3/2}. \tag{1.11}$$

The additional factor 3 accounts for multiple pockets. Taking the derivative of (1.11) with respect to energy, the density states is obtained as

$$D(E) = \frac{1}{V}\frac{\mathrm{dN}}{\mathrm{dE}} = \frac{3\sqrt{2}}{\pi^2\hbar^3} \left(m_x m_y m_z\right)^{\frac{1}{2}} \left(\frac{E^2}{E_g} - E\right)^{\frac{1}{2}} \left(\frac{2E}{E_g} - 1\right). \tag{1.12}$$

The energy dependence of the non-parabolic density of states differs drastically from the valence band density of states (1.9). The difference is illustrated in figure 1.3, where both are plotted at 77 and 300 K.

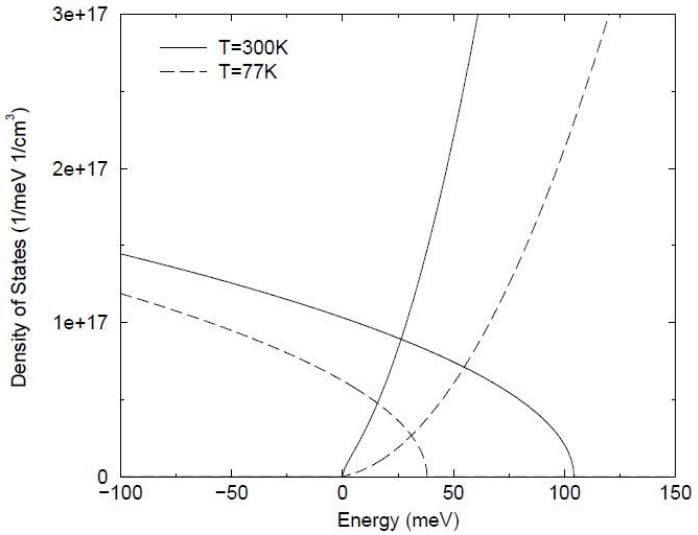

Figure 1.3: Bulk density of states of the L-point conduction band and the T-point valence band plotted together at 77 and 300 K. The zero energy is taken as the bottom of the L-point conduction band [7].

1.2 Overview of classical magnetotransport

The basic principles of classical or semiclassical magnetotransport theory are reviewed following the notation of Pippard [12]. Expressions for the magnetoresistance and Hall coefficient for a two carrier metal for the extraction of carrier mobilities and concentrations are presented, and their applicability to bismuth is discussed.

Being a semimetal, bismuth has favorable properties for exhibiting very large ordinary magnetoresistance (MR), already in *classically* strong fields. This means that Landau quantization is still negligible, and quantum magneto-oscillations have not yet manifested. Ordinary magnetoresistance is caused by the curving of the electron trajectories in a magnetic field due to the Lorentz force.

Let's consider electrons in a Fermi gas with approximately spherical Fermi surface. The conductivity or resistivity are given by the formulae

$$\sigma_0 = ne^2\tau/m^* \quad \text{and} \quad \rho_o = m^*/ne^2\tau, \tag{1.13}$$

where n is the electron concentration and m* is the effective mass. The relaxation time τ is a time-constant that describes the time for a current to vanish when an applied

electric field is removed. When a magnetic field **B** is introduced, the trajectory of electrons is bent to helices due to the Lorentz force e(**v**×**B**). If the path of electrons is appreciably changed by the magnetic field during the free path between collisions, the conductivity changes. This effect is called magnetoresistance, which can be either positive or in some cases even negative.

The Lorentz force bends the electron paths into helices whose axes are parallel to **B**. The angular velocity of an electron round its particular axis is described by the cyclotron frequency

$$\omega_c = eB/m^*. \tag{1.14}$$

At a given value of **B**, cyclotron frequency is an intrinsic property of the material. The product $\omega_c\tau$ describes the mean angle the electron turns between collisions. A central requirement for having any appreciable magnetoresistance effect is the condition $\omega_c\tau > 1$. Combining the two expressions above,

$$\omega_c\tau = \frac{B\sigma_o}{ne}, \tag{1.15}$$

which allows to estimate the magnitude of $\omega_c\tau$. Starting with with copper at 0 ℃, in a very strong magnetic field of 30 T, $\omega_c\tau$ is only 0.14 and very weak effect is observed. If the temperature is lowered to 4 K, so that the conductivity increases with a factor of roughly 600, $\omega_c\tau$ is 28 at 10 T field. The electrons now execute about 4 turns between collisions, and the conductivity process changes considerably. At these conditions, the resistivity of copper increases 14-fold.

The above simple analysis can be extended also to bismuth, although its Fermi surface is far from spherical. Bismuth has an electron density lower than copper approximately by a factor of 10^5, but resistivity only about 70 times more (evidence of an unusually long mean free path or relaxation time), and by applying equation (1.14), one gets $\omega_c\tau \sim 20\mathrm{B[T]}$. Thus even at room temperature, bismuth shows considerable MR effects. Bulk bismuth is an almost fully compensated metal (equal number of holes and electrons) which enhances the MR effects even more. When cooled down to 4.2 K, bismuth has its resistivity increased by several million times in a 10 T field. Thus a field of 1 mT was sufficient to bring $\omega_c\tau$ to unity.

Electron accelerated by an electric field $\mathcal{E}$ moves according to equation

$$m^*\dot{\mathbf{v}} = e\mathcal{E}. \tag{1.16}$$

The current density rises steadily, if the electrons are not deflected and their motion is randomized:

$$\dot{\mathbf{J}} = \sum e\dot{\mathbf{v}} = ne^2\mathcal{E}/m^*. \tag{1.17}$$

The summation is taken over all electrons in unit volume. When $\mathcal{E}$ is removed, $\mathbf{J}$ decays exponentially due to collisions. This is a good approximation for an isotropic degenerate gas, and fairly good for a Boltzmann gas. Now (1.17) is written as

$$\dot{\mathbf{J}} = ne^2\mathcal{E}/m^* - \mathbf{J}/\tau. \tag{1.18}$$

τ is assumed to have the same value for all directions of $\mathbf{J}$. In a steady state $\dot{\mathbf{J}} = 0$, and $\mathbf{J}$=$\sigma_0\mathcal{E}$. We can now consider the momentum balance in the electrons gas. the momentum density $\mathbf{P}$=$\sum m^*\mathbf{v} = m^*\mathbf{J}/e$, and (1.18) becomes

$$\dot{\mathbf{P}} = ne\mathcal{E} - \mathbf{P}/\tau. \tag{1.19}$$

The momentum density is changed by electrical force density $ne\mathcal{E}$ and collisional term -$\mathbf{P}/\tau$. In the steady state they balance. Now we apply $\mathbf{B}$ transverse to $\mathbf{J}$, exerting a Lorentz force $e\mathbf{v}\times\mathbf{B}$ on each electron and a force density $\sum e\mathbf{v}\times\mathbf{B}$, which equals $\mathbf{J}\times\mathbf{B}$ on the electron assembly as a whole. Adding this to (1.19), in the steady state we have

$$0 = ne\mathcal{E} - \mathbf{P}/\tau + \mathbf{J}\times\mathbf{B} = ne\mathcal{E} - m^*\mathbf{J}/e\tau + \mathbf{J}\times\mathbf{B}. \tag{1.20}$$

This force balance is represented as a vector diagram in fig. 1.4. Assumptions are that τ and m* are unaffected by B, which is almost always a valid assumption. It can be seen that the component of $\mathcal{E}$ *parallel* to J is unchanged, but a transverse component arises to cancel the Lorentz force. Thus a free (or quasi-free) electron gas shows no magnetoresistance. This is evident in potassium, in which the Fermi surface is very close to spherical and represents the free electron model quite accurately; the magnetoresistance effect is very weak.

The transverse component of $\mathcal{E}$ is called the Hall field, with magnitude JB/ne. It is measured as a transverse voltage drop in an experiment where current is passed through a wire or strip in the presence of magnetic field. In this case $\mathcal{E}$ adjusts itself with the help of space charges or surface charges to satisfy (1.20). The Hall angle is defined as the angle between $\mathbf{J}$ and $\mathcal{E}$, as

$$\tan\varphi = eB\tau/m^* = \omega_c\tau, \tag{1.21}$$

using (1.14). The quantity $e\tau/m^*$ is often written as the mobility μ, which relates the electric field to drift velocity as $\mathbf{v} = \mu\mathcal{E}$.

1.2.1 Magnetoconductivity and magnetoresistivity tensors

In experiments the magnitude and direction of $\mathbf{J}$ is fixed, and $\mathcal{E}$ responds accordingly. The measured quantity is the resistivity tensor

$$\mathcal{E}_i = \rho_{ij}J_j. \tag{1.22}$$

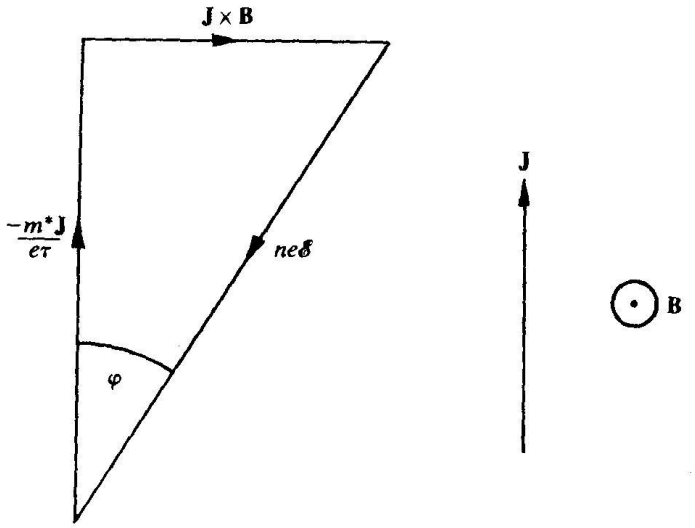

Figure 1.4: Forces acting on a unit volume of quasi-free electron gas carrying current **J** in transverse field **B** [12].

For theoretical purposes it can be useful to think in terms of conductivity, so that $\mathcal{E}$ is the fixed quantity. The conductivity tensor is thus

$$J_i = \sigma_{\mathrm{ij}}\mathcal{E}_j. \tag{1.23}$$

The measured quantity can be a component or combination of components from the conductivity or resistivity tensor. The relation between σ_{ij} and its inverse ρ_{ij} is

$$\rho_{\mathrm{ii}} = (\sigma_{\mathrm{jj}}\sigma_{\mathrm{kk}} - \sigma_{\mathrm{jk}}\sigma_{\mathrm{kj}})/\,\Delta(\sigma) \;\; ; \;\; \rho_{\mathrm{ij}} = (\sigma_{\mathrm{ik}}\sigma_{\mathrm{kj}} - \sigma_{\mathrm{ij}}\sigma_{\mathrm{kk}})/\,\Delta(\sigma), \tag{1.24}$$

where $\Delta(\sigma)$ is the determinant of the tensor σ. Similarly,

$$\sigma_{\mathrm{ii}} = (\rho_{\mathrm{jj}}\rho_{\mathrm{kk}} - \rho_{\mathrm{jk}}\rho_{\mathrm{kj}})/\,\Delta(\rho) \;\; ; \;\; \sigma_{\mathrm{ij}} = (\rho_{\mathrm{ik}}\rho_{\mathrm{kj}} - \rho_{\mathrm{ij}}\rho_{\mathrm{kk}})/\,\Delta(\rho). \tag{1.25}$$

In presence of magnetic field B, σ_{ij} and ρ_{ij} are not symmetrical, but require all nine elements for complete description. Usually, **J** and **B** are applied in particular directions, i.e. **B**=B_z and **J**=J_x. Almost always, the longitudinal to transverse coupling is negligible, so that we can set the components σ_{xz}, σ_{zx}, σ_{yz}, and σ_{zy} to zero. Now (1.24) is written as

$$\begin{aligned} &\rho_{\mathrm{xx}} = \sigma_{\mathrm{yy}}/\Delta'(\sigma), \quad \rho_{\mathrm{yy}} = \sigma_{\mathrm{xx}}/\Delta'(\sigma), \quad \rho_{\mathrm{zz}} = \frac{1}{\sigma_{\mathrm{zz}}}, \\ &\rho_{\mathrm{xy}} = \sigma_{\mathrm{xy}}/\Delta'(\sigma), \quad \rho_{\mathrm{yx}} = -\sigma_{\mathrm{yx}}/\Delta'(\sigma), \end{aligned} \tag{1.26}$$

where

$$\Delta'(\sigma) = \sigma_{\mathrm{xx}}\sigma_{\mathrm{yy}} - \sigma_{\mathrm{xy}}\sigma_{\mathrm{yx}}.$$

Inversion of ρ_{ij} to σ_{ij} proceeds correspondingly, from (1.25).

When B is applied in the z - direction and $\mathcal{E}$ in x - direction, the induced current density will be $\mathbf{J}$=$\sigma_0\mathcal{E}_x\hat{x}$. Resulting Hall field will be in according to (1.21) $\mathcal{E}_y = (\omega_c\tau)\mathcal{E}_x$. The definition $\mathbf{J} = \sigma \cdot \mathcal{E}$,

$$\begin{pmatrix}\sigma_0\\0\\0\end{pmatrix}\mathcal{E}_x = \sigma \cdot \begin{pmatrix}\mathcal{E}_x\\(\omega_c\tau)\mathcal{E}_x\\0\end{pmatrix}, \tag{1.27}$$

will yield

$$\sigma = \begin{pmatrix}\frac{\sigma_0}{1+(\omega_c\tau)^2} & \frac{\sigma_0\omega_c\tau}{1+(\omega_c\tau)^2} & 0\\ \frac{-\sigma_0\omega_c\tau}{1+(\omega_c\tau)^2} & \frac{\sigma_0}{1+(\omega_c\tau)^2} & 0\\ 0 & 0 & \sigma_{zz}(0)\end{pmatrix} = \begin{pmatrix}\frac{\sigma_0}{1+\gamma^2} & \frac{\sigma_0\gamma}{1+\gamma^2} & 0\\ \frac{-\sigma_0\gamma}{1+\gamma^2} & \frac{\sigma_0}{1+\gamma^2} & 0\\ 0 & 0 & \sigma_{zz}(0)\end{pmatrix}, \tag{1.28}$$

where $\gamma = \omega_c\tau$. The resistivities are $\rho_{xx} = \rho_{yy} = 1/\sigma_0$ and $\rho_{xy} = -\rho_{yx} = \omega_c\tau/\sigma_0$. The Hall coefficient R_H is defined as

$$R_H = -\frac{\sigma_{xy}}{B_z}, \tag{1.29}$$

so that the negative sign is taken for free electrons and for any conductor in which Hall angle φ has the same sign as a free electron metal.

For calculations, treating the plane normal to $\mathbf{B}$ as a complex plane in which $\mathbf{J}$ and $\mathcal{E}$ are complex numbers is sometimes useful. By introducing the notation $\sigma_1 = \sigma_{\mathrm{xx}} = \sigma_{\mathrm{yy}}$, $\sigma_2 = \sigma_{\mathrm{xy}} = -\sigma_{\mathrm{yx}}$, and $\sigma_3 = \sigma_{\mathrm{zz}}$, so that

$$\sigma_{ij} = \begin{pmatrix}\sigma_1 & \sigma_2 & 0\\ -\sigma_2 & \sigma_1 & 0\\ 0 & 0 & \sigma_3\end{pmatrix}. \tag{1.30}$$

Now $\mathcal{E}$ and $\mathbf{J}$ are linearly related by complex σ or ρ, $\sigma_{2D} = \sigma_1$–iσ_2 and $\rho_{2D} = \rho_1$–iρ_2. These expressions describe the conductivity and resistivity in the xy-plane, and are valid when magnetic field is in the z-direction and no transverse-longitudinal coupling is assumed. The negative sign arises because $\mathrm{J}_y = \sigma_{xy}\mathcal{E}_x = \mathrm{Im}[\sigma\mathcal{E}]$. Now the inversion of ρ into σ can be calculated by complex algebra as

$$\rho_{2D} = 1/\sigma_{2D} = \frac{\sigma_1 + \mathrm{i}\sigma_2}{\sigma_1^2 + \sigma_2^2}, \tag{1.31}$$

so that $\rho_1 = \sigma_1/(\sigma_1^2 + \sigma_2^2)$ and $\rho_2 = -\sigma_2/(\sigma_1^2 + \sigma_2^2)$ in agreement with (1.26). For a free electron metal for which $\gamma = \omega_c\tau > 0$,

$$\rho_{2D} = \rho_0/(1 - \mathrm{i}\gamma) \quad \text{and} \quad \sigma_{2D} = \sigma_0/(1 - \mathrm{i}\gamma). \tag{1.32}$$

1.2.2 Extension for two a carrier metal

In semiconductors, the electrons excited from the valence band to the conduction band leave behind an empty state, which is referred to as a hole. This electron absence can contribute to conduction, especially in materials where Fermi level lies within the conduction band. Holes can be treated as charge carriers with charge +e and different effective mass m_h^*. In the free electron theory, we can treat it as a classically behaving particle, with a concentration p and with a conductivity σ_h=$pe^2\tau_h/m_h^*$=$pe\mu_h$. In the presence of magnetic field **B**, both electrons and holes would behave according to (1.32). Therefore the total conductivity is

$$\sigma_{2D} = \sigma_e/\left(1 - \mathrm{i}\gamma_e\right) + \sigma_h/\left(1 + \mathrm{i}\gamma_h\right), \tag{1.33}$$

where γ is written for $|\omega_c\tau|$, as the opposite sign of the charges is reflected in the sign of the denominator. By using (1.15), the equation above is written as

$$\sigma_{2D} = \frac{ne}{B}\left(\frac{\gamma_e}{1 - \mathrm{i}\gamma_e} + \frac{c\gamma_h}{1 + \mathrm{i}\gamma_h}\right), \tag{1.34}$$

where $c = p/n$. For a compensated metal c=1.

The resistivity ρ is $1/\sigma$, and by inverting (1.34) one obtains

$$\rho_{2D} = \frac{B}{ne}\frac{(\gamma_e + c\gamma_h + \gamma_e\gamma_h(\gamma_h + c\gamma_e)) - \mathrm{i}(\gamma_e^2 - c\gamma_h^2 + (1-c)^2\gamma_e^2\gamma_h^2)}{(\gamma_e + c\gamma_h)^2 + (1-c)^2\gamma_e^2\gamma_h^2}. \tag{1.35}$$

The real part of equation (1.35) describes magnetoresistance, and the imaginary part describes Hall resistivity. One can then write $\rho_0 = (\sigma_e + \sigma_h)^{-1} = 1/en(\mu_e + c\mu_h)$ in terms of mobilities, and since $\omega_c\tau = \mu B$, the following expression is obtained:

$$r = \frac{\rho(B)}{\rho_o} = \frac{R(B)}{R(0)} = \frac{1 + \mu_e\mu_h\frac{\mu_h + c\mu_e}{\mu_e + c\mu_h}B^2}{1 + (1-c)^2\frac{\mu_e^2\mu_h^2}{(\mu_e + c\mu_h)^2}\mathrm{B}^2}, \tag{1.36}$$

where $\mu_e = e\tau_e/m_e^*$ and $\mu_h = e\tau_h/m_h^*$. Equation (1.36) describes classical magnetoresistance, which is quadratic at low fields, and depending on the value of c, saturates at high fields. If c = 1, quadratic rise continues indefinitely. The high and low field limits of (1.36) are

$$\begin{aligned} r &\sim 1 + \frac{c\mu_e\mu_h(\mu_e + \mu_h)^2}{(\mu_e + c\mu_h)^2}B^2 && \text{for } B \to 0 \\ r &\sim \frac{1 + c(\mu_e/\mu_h + \mu_h/\mu_e) + c^2}{(1-c)^2} && \text{for } B \to \infty. \end{aligned} \tag{1.37}$$

The behavior of (1.36) at different values of c is plotted in figure 1.5. Note that expression (1.36) is symmetric for the inversion of c, so that changing c to 1/c result in a same curve.

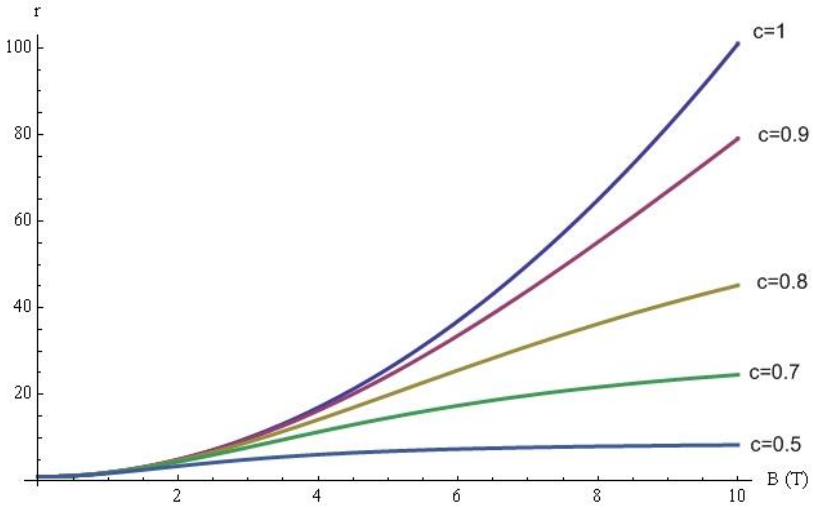

Figure 1.5: Classical magnetoresistance for a two carrier metal plotted with different values of c ($\mu_e = \mu_h = 1$).

The expression for Hall coefficient $R_H = \rho_{xy}/B$ can be obtained similarly, from the imaginary part of (1.35):

$$R_{Hall} = -\frac{1}{n|e|}\frac{\mu_e^2 B^2 - c\mu_h^2 B^2 + (1-c)^2 \mu_e^2 B^2 \mu_h^2 B^2}{(\mu_e B^2 + c\mu_h B^2)^2 + (1-c)^2 \mu_e^2 B^2 \mu_h^2 B^2}. \tag{1.38}$$

The behavior of (1.38) is plotted in figure 1.6. In the limit of high and low fields, (1.38) becomes

$$\begin{aligned} R_{Hall} &\sim -\frac{\frac{1}{n|e|}}{1-c} && \text{for } B \to \infty \\ R_{Hall} &\sim -\frac{1}{n|e|}\frac{\mu_e^2 - c\mu_h^2}{\mu_e + c\mu_h} && \text{for } B \to 0. \end{aligned} \tag{1.39}$$

Equations (1.38) and (1.39) yield interesting predictions. First of all, the Hall coefficient has significant field dependency, in contrast to a single carrier metal where it is constant. Moreover, the sign of the Hall coefficient depends not only on the majority carrier type, but also on the mobilities of the carriers. This can be seen from the term $(\mu_e^2 - c\mu_h^2)$ in the low field limit expression. Bulk bismuth is approximately compensated, and electrons considerably more mobile, so that sign of the Hall coefficient reflects the electronic conductance. In thin films, however, the compensation is not necessary perfect, and the mobilities might have very different values for various reasons, because of impurities or smaller grain size etc.

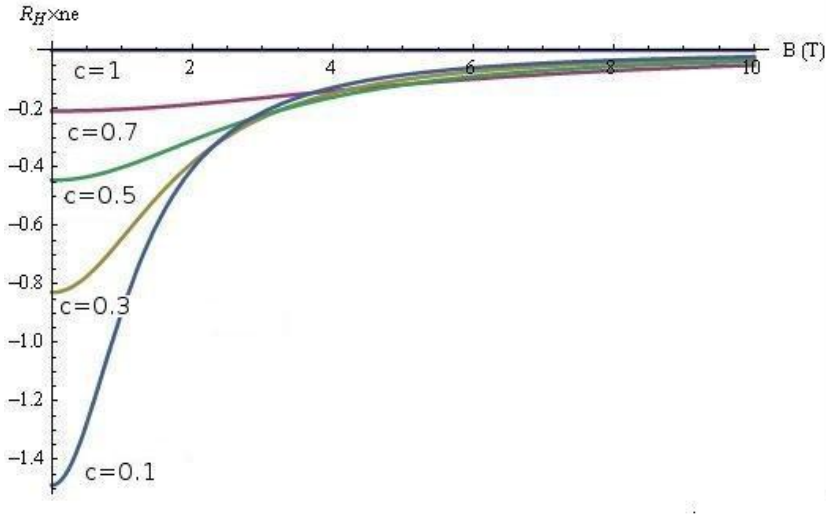

Figure 1.6: Hall coefficient (1.38) plotted with different values of c ($\mu_e = \mu_h = 1$).

Equations (1.36) and (1.38) could in principle be used to extract carrier mobilities and carrier concentrations from the measured magnetoresistance and Hall coefficient data. In practice however, it turned out that as these expressions have three or four free fitting parameters (μ_e, μ_h, c, n), the numerical algorithms used for the fitting of the curves do not converge properly. This is simply because there are too many free parameters, and moreover the parameters depend heavily on each other (products $\mu_e\mu_h$ etc.).

The following calculation shows how a two parameter fit (μ_e, μ_h) for magnetoresistance can be derived. By multiplying the zero field conductivity

$$\sigma_0 = en(\mu_e + c\mu_h), \tag{1.40}$$

and the low field Hall coefficient (1.39), we can define a new constant A

$$\sigma_0 R_{Hall}(0) = en(\mu_e + c\mu_h) \cdot -\frac{1}{n|e|}\frac{\mu_e^2 - c\mu_h^2}{\mu_e + c\mu_h} = -\frac{\mu_e^2 - c\mu_h^2}{\mu_e + c\mu_h} \equiv A, \tag{1.41}$$

so that the carrier concentration ratio c can be solved as

$$c = \frac{-A(\mu_e + \mu_e^2)}{(A - \mu_h)\mu_h}. \tag{1.42}$$

The quantity $\mathrm{R}_{Hall}(0)$ is obtained from the experimental data as

$$R_{Hall}(0) = \frac{dV_{Hall}}{dB}\frac{t}{I}, \tag{1.43}$$

where the derivative is taken at the low field region where Hall voltage is still linear, t is the thickness of the sample, and I is the bias current. By plugging (1.42) into (1.36), one obtains an equation for magnetoresistance with only two fitting parameters μ_e, μ_h.

$$r = \frac{1 + (\mu_e^2 + \mu_h^2 - \mu_e\mu_h + A(\mu_e - \mu_h))B^2}{1 + (A + \mu_e - \mu_h)^2 B^2}. \tag{1.44}$$

Applying the model above for bismuth is an approximation, neglecting e.g. electron anisotropies. However, bismuth thin films usually contain small grains in multiple orientations, so that the transport properties are averaged. Thus the isotropic two carrier model gives at least a rough estimate for the average mobilities. In addition it works better in low fields, since in bulk bismuth the quadratic rise in magnetoresistance have been shown to continue almost to $\rho(B)/\rho_0 \approx 10^6$ [13], in a field of about 10 T.

Chapter 2

Experimental Methods

The bismuth samples were fabricated in the Nanoscience Center cleanroom in University of Jyväskylä. Standard microfabrication methods were used, which are described in detail by several authors, e.g. [14–16]. Thus, here only the specific parameters used in sample fabrication are mentioned.

2.1 Methods previously used for bismuth thin film growth

The aim of this work was to fabricate bismuth thin films with high crystal quality, i.e. films with large grain size. Fabrication of truly single-crystal films seems to be very difficult. Several different approaches have been applied in earlier studies, which are briefly reviewed here. In general, a few different deposition techniques have been utilized, special substrates have been shown to improve crystal quality, and finally post deposition thermal annealing has a significant effect on the film quality.

The deposition methods used include Molecular Beam Epitaxy (MBE), electrodeposition, and vapor deposition methods. MBE produces epitaxial films, with metallic resistivity temperature dependence, high magnetoresistance, high mobilities, and the films exhibit e.g. Shubnikov-de Haas oscillations [17–19]. The downside of MBE is that it is an expensive and slow technique, and thus unsuitable for large scale production. Electrodeposition and vapor deposition (thermal evaporation, sputtering) are faster and more economical deposition methods, which are also compatible with standard lithography methods. Electrodeposition combined with post-deposition annealing produces high quality films [20–22]. Finally, vacuum evaporated and postannealed bismuth films have metallic resistivity behavior and large magnetoresistance [23], although not quite as high as for films grown with other methods.

Lattice matched substrates have been shown to produce higher crystallinity in Bi films. CdTe(111) and BaF_2(111) substrates have small lattice mismatch (0.7 % and 3.6 % in trigonal direction, respectively), and have been frequently used for the MBE

grown films. Another special substrate is the mineral Muscovite Mica, which has a sheet structure and it can be cleaved to produce atomically flat surfaces. CdTe and BaF_2 are somewhat expensive materials, whereas Mica can be obtained at a reasonable price. Bismuth films on Mica grow in the preferred (001) orientation [24]. The transport properties of bismuth films grown on Mica have been studied in several occasions, where the films are claimed to have epitaxial structure [25, 26].

The crucial step in the film fabrication, regardless of the deposition method, seems to be the thermal treatment during and after the film growth. This is true even for the MBE grown films, and thermal annealing has even larger relative effect on the films grown with other methods. It seems that heating the substrate to around 130 ℃ promotes growth of larger crystals during deposition. Films grown by MBE and kept at ambient temperature showed inferior properties compared to those grown on elevated temperatures. Thermal annealing of these films after the deposition greatly improved their properties. The power of post deposit annealing is evident in the electrodeposited films, where the annealing substantially increases the magnetoresistance of the films, and changes the resistivity behavior to more or less metallic as well. Even films grown on glass substrates show metallic resistivity, when subjected to suitable thermal treatment [23].

The electrodeposited films have an Au underlayer that serves as a working electrode during the deposition. Recently, it was shown that films grown on glass substrate by thermal evaporation with predeposited thin gold layer show high magnetoresistance and low resistivity after thermal annealing [23]. It was shown that the gold diffuses into bismuth and contributes to the grain growth. The same process is likely to happen in the annealed electrodeposited films, which could be the reason for their good quality. This is an interesting finding, since this mechanism for the bismuth film improvement might work for films grown on standard oxidized silicon substrates.

2.2 Sample fabrication

Majority of work focusing on electrodeposited and vacuum deposited bismuth films has been done with film thickness ranging from 1 to 20 µm. In this thesis the effectiveness of post deposition annealing process is studied with much thinner films, with thickness ranging from 65 to 380 nm. The quality of the bismuth films grown on standard oxidized silicon and on Muscovite Mica substrates are compared. Also the effect of the Au underlayer is studied with thin (65 and 125 nm) bismuth films, grown on SiO_x substrates. The films studied here are fabricated using standard lithographic processes with high vacuum e-beam metal evaporation, since in real applications it is beneficial that the fabrication process itself is as compatible as possible with standard patterning and microfabrication processes.

Muscovite Mica structure and properties

The mica minerals are phyllosilicates (or sheet silicates) with a common basic crystal structure [27]. The mineral group is composed of 41 species and seven mineral series. 6 out these are rock forming minerals, Muscovite and Biotite being the most common forms. Muscovite Mica has the composition $KAl_2(Si_3Al)O_{10}(OH,F)_2$.

Micas have sheet structure whose basic units consist of two polymerized sheets of silica (SiO_4) tetrahedrons. Two sheets are juxtaposed with the vertices of the tetrahedrons pointing toward each other, and the sheets are cross-linked with cations (e.g. Al in muscovite). The cross-linked double layer is bound firmly. These double layers are joined via singly charged cations (potassium in muscovite) to form the complete structure (figure 2.1).

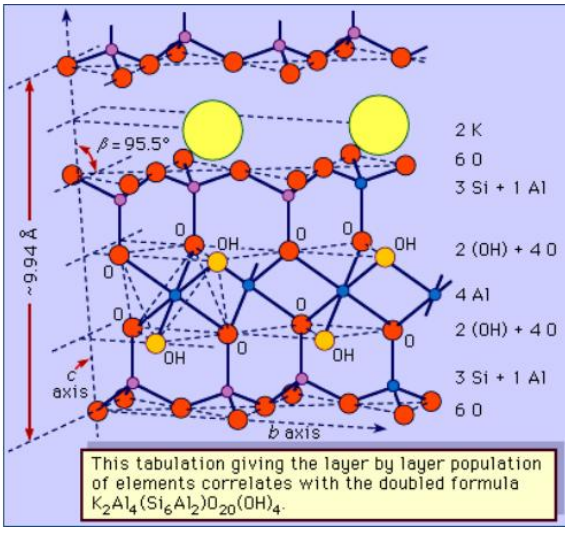

Figure 2.1: Muscovite Mica structure, showing the double layer sheet unit [28].

Muscovite mica has a low electric and thermal conductivity and high dielectric strength. It exhibits perfect cleavage in the basal (001) plane due to the sheet structure described above. Mica sheets have been used in electrical condensers, insulating elements, in optical instruments, and as a calibration aid in atomic force microscopy (AFM).

2.2.1 Lithography

Muscovite Mica was obtained from Electron Microscopy Sciences. The mica used was the highest V-1 quality purchased as 50 × 75 mm sheets with thickness of 0.15 –0.21 mm. The mica was cut to a 1 cm × 1 cm pieces with a silicon saw. Mica is a very brittle material that scratches easily. The mica sheet was placed between two adhesive sheets (standard dicing tape, medium blue tack from Semiconductor Equipment Corp.) for the cutting. After the cutting was done, the mica and the adhesive sheet was immersed

in acetone to gently remove the adhesive. If the adhesive was directly peeled off, the mica pieces could cleave into thinner pieces even though the adhesive tape was only weakly adhesive. The mica chips were cleaned in hot acetone in an ultrasonic bath, after which they were rinsed in isopropanol (IPA) and blow dried with N_2. The pieces were inspected and the ones damaged by the cutting process were sorted out.

Boron doped standard silicon wafer was thermally oxidized in a tube furnace. The furnace was heated to 800 ℃, and oxygen gas was flown through the chamber at atmospheric pressure for 8 hours. The wafer was cut with a diamond cutter into smaller chips. The chips were subsequently cleansed in hot acetone immersed in ultrasonic bath. The surface was gently scrubbed with cotton pad applicators. The chips were then rinsed in IPA and blow dried with N_2.

The sample geometry in shown in figure 2.3. Conventional Hall bar geometry was used, the width of the film was around 10 µm and the length about 1 mm. Because the mica is a dielectric so that electron beam lithography is a bit complicated, photolithographic process was used in the sample fabrication.

Template for the photo-mask was a microscope glass coated with 100 nm aluminum by vacuum evaporation in a Balzers Bal-Tec Bae250 high vacuum evaporator. After the evaporation, 4 % PMMA in anisole was spun with 2000 rpm for 45 s and then baked for 3 minutes at $\sim$ 160℃. The Hall bar pattern was designed with Elphy Quantum 1.3 lithography software and was patterned with Leo 1430 scanning electron microscope (SEM). The resist was subsequently developed in methyl isobutyl ketone (MIBK) and isopropanol (IPA) (1:3 v/v) for 45 s and rinsed in IPA, followed by drying in nitrogen flow. The exposed aluminum was wet etched in 1.4 % (by weight) NaOH solution for about 90 s, and cleansed in deionized water.

The schematic of the photolithographic process is shown on figure 2.2. The first resist layer spun on the chips was Microchem PMGI [29]. It was spun with 2500 rpm on the mica samples and with 3500 rpm on SiO_x, for 45 s. The resist was baked for

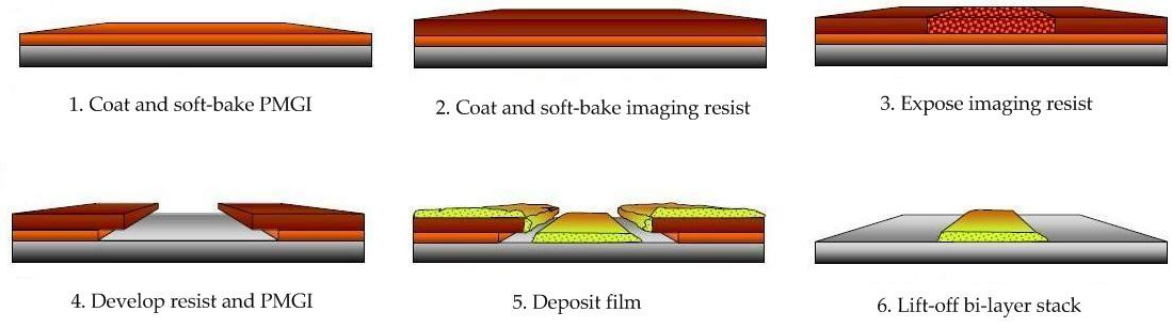

Figure 2.2: Schematic of the lithographic process used in the sample fabrication [29]

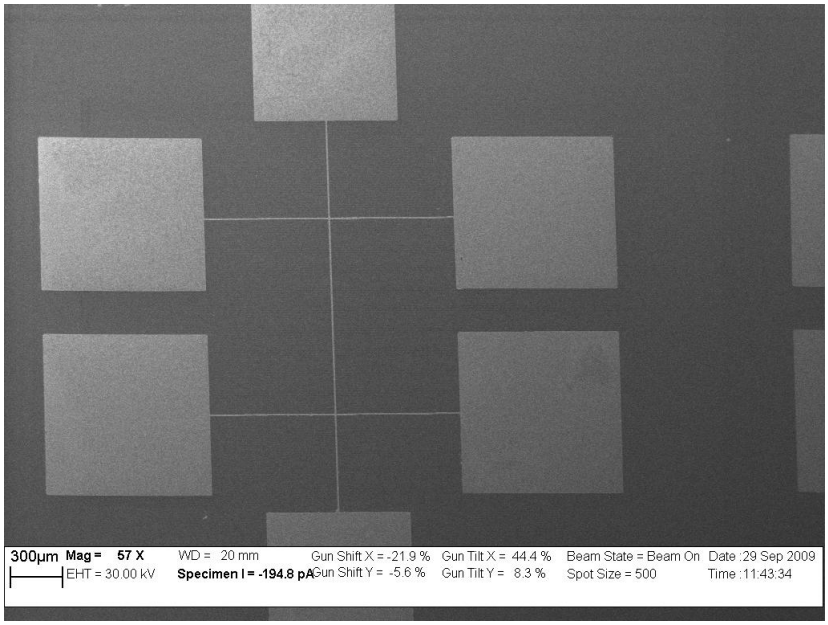

Figure 2.3: SEM image of a bismuth sample grown on SiO_x.

2 minutes on a hot plate at $\sim$ 160℃. Another resist layer was spun on top of that, the UV sensitive AZ1514H with 3500 rpm for 45 s. The photoresist was baked for 1 minute at $\sim$ 110 ℃ on a hot plate. After baking, the resist was exposed through the photo-mask with Karl-Suss 45MA mask-aligner for 45 s and developed in AZ 351B developer (mainly buffered NaOH) for 60 – 90 seconds. It was found that the 351B developer also dissolves the PMGI, so that it could be used to dissolve the bottom resist layer to form an undercut profile to assist in the lift-off. After developing, the chips were rinsed in deionized water and blow dried with N_2.

The metal evaporation was done in the Bae250 high vacuum e-beam evaporator, with a base pressure of $\sim 5 \times 10^{-6}$ mbar. Bismuth was obtained from Goodfellow Inc. at 99.9999 % purity, and was evaporated at a rate of 2-3 Å/s. Thickness of the evaporated layer was monitored with quartz crystal microbalance, and the real thickness determined via AFM measurements. The lift-off was done in hot acetone, with a brief sonication to ensure complete lift-off. After that the chips were again rinsed in IPA and dried. The acetone did not dissolve completely the PMGI, but the extra resist layer was left on the chip. An SEM image of a typical sample is shown on figure 2.3.

2.2.2 Annealing process

The annealing was done in vacuum chamber with a base pressure below 5×10^{-4} mbar. The heating element was a cylindrical boraelectric heater, with an inner diameter on about 2 cm and a length of about 10 cm. The sample was mounted on a ceramic sample

stage, with a 2 mm thick copper plate beneath it. The temperature of the sample stage was monitored with a thermocouple, and the heating element had its own thermocouple connected to the Tectra HC 3500 heater controller. The heater was controlled with a PID controller. 2-wire resistance measurements were done *in-situ* during the annealing, with mechanical copper clamp contacts on the sample.

It has been previously established that an annealing temperature of 270 ℃ is needed for the pure bismuth films, and an annealing time of 10 h for complete annealing [31]. The grain size was shown to increase exponentially in the range 266 – 270 ℃, which means that very careful temperature control in the vicinity of bismuth melting point is needed. Temperature higher than the melting point leads to agglomeration and discontinuity of the film.

Since the annealing was done in a vacuum, the heat was transported to the sample mainly by radiation. It was found that there was a notable heat gradient in the sample stage, as the heat was conducted away from the stage via the rod holding the sample stage. This was evident in the mica samples, as the second sample in the chip "deeper" in the cylindrical oven melted and the other one stayed intact. The sample was covered with a copper shield to help maintain it in thermal equilibrium with the surroundings. Nevertheless, the temperature control was somewhat difficult. As the silicon substrates were better heat conductors, less gradient was present in these samples. The samples grown on SiO_x needed considerably higher temperature setpoint (about 10 ℃) to reach the melting temperature.

The melting point of the samples were determined by trial-and-error, since the thermocouple attached to the sample stage did not measure the actual temperature of the sample. The melting of the sample was seen as a loss of electrical conductivity in the resistance measurement. The optimum annealing temperature was thus found by setting the heater controller to a value slightly below the observed melting point. Annealing was done for 8 – 10 h, which seemed sufficient, since a further annealing period of 6 h did not cause further change in the room temperature resistance.

The annealing procedure for the AuBi samples is somewhat different. The studied samples had 3/122 nm and 2/48 nm thicknesses of gold/bismuth deposited on SiO_x substrate, in similar ratios as in [23]. It was shown in [23] that the gold diffuses into the bismuth, and is thought to facilitate grain boundary motion and growth. The phase diagram of Au-Bi system is shown on figure 2.4. Annealing starts to be effective above the eutectic point 241 ℃, and the melting point of the Au-Bi system depends on the percentage of bismuth in the alloy. The annealing temperature is within this interval. Above the eutectic point, the gold enters a liquid phase, and can diffuse into the bismuth. Again the optimal annealing temperature was determined experimentally.

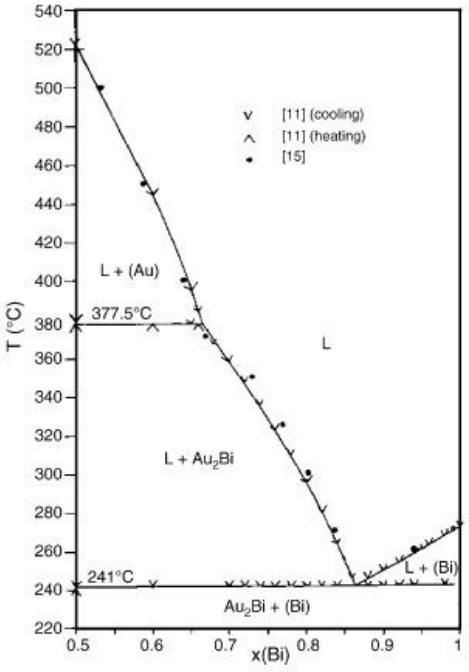

Figure 2.4: Phase diagram of Bi-Au binary system [30].

2.3 Measurements

The electrical properties of the samples were determined by resistivity measurements between 4.2 and 295 K, and with magnetoresistance and Hall measurements at 4.2 K.

The samples were mounted on the sample stage using CMR 7031 varnish. The contact pads on the samples were deliberately made very large (about 1 mm $\times$ 1 mm), since the electrical contacts had to be "cold-soldered" with indium. Bismuth is such a soft material, and especially on mica substrate the surface is too fragile to be ultrasonically bonded. A small piece of indium was melted on the end of a copper wire, and it was pressed with a scalpel tip onto the contact pad. The indium stuck surprisingly well onto the bismuth surface, and the contact area was quite large. The temperature sensor mounted on the sample stage was a Rhodium-Iron RF-100 sensor obtained from Lakeshore.

The magnet used in the measurements was a home-built cylindrical superconducting coil magnet, producing a field up to $\sim$ 3.5 T. The magnet was first cooled in liquid nitrogen (LN_2), and then lowered into a liquid helium (LHe) dewar into the helium bath.

The sample stage was mounted at the end of an dip-stick, which had an open structure without vacuum. The dip-stick was first lowered into liquid nitrogen (77 K) and then slowly lowered into LHe dewar, and slowly cooled down to 4.2 K. The helium

bath was freely boiling at atmospheric pressure. The resistance of the thermometer was measured with AVS resistance bridge, and the sample was measured with Stanford SRS 810 lock-in amplifier with a low frequency AC mode with current bias, with frequency f = 17 Hz and R_0 = 5 MΩ, as shown on figure 2.5. The resistivity versus temperature was recorded during the slow warming up, by lifting the sample very slowly from the helium bath. The warming up to room temperature was done in a course of 4 - 5 hours.

The magnetoresistance was measured with the same setup. The magnetic field was slowly swept from zero to 3.5 T and back. Too fast a sweep would produce slightly hysteretic data. The field was swept in both directions by reversing the polarity of the current through the magnet.

The Hall measurements were done by measuring the transverse voltage drop as a function of the magnetic field. Ithaco 1201 voltage amplifier with a gain of G = 1K was used to amplify the Hall voltage. Because in real samples the opposing arms in the Hall bar (fig. 2.3) cannot be perfectly aligned, there is an offset in the Hall voltage at zero field caused by the coupling of the longitudinal resistance to the transverse. To eliminate the offset voltage, the field was swept in both directions and Hall voltage was taken as the average

$$V_H = 1/2(V_{xy}(B) - V_{xy}(-B)). \tag{2.1}$$

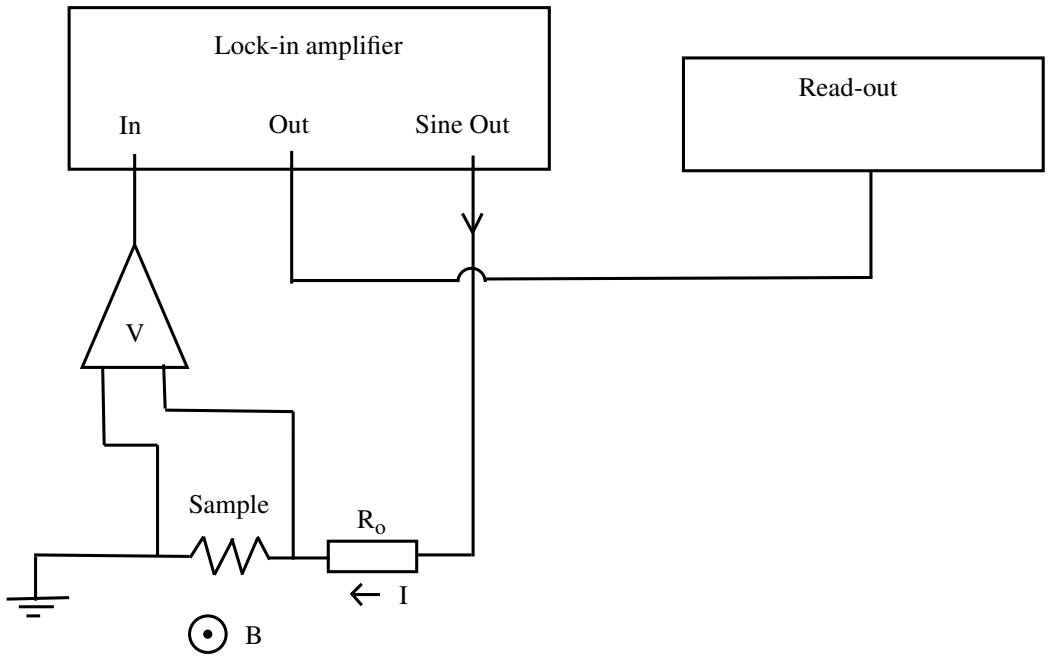

Figure 2.5: Schematics of the setup for resistivity and magnetoresistance measurements. The Hall measurement setup is identical except that the transverse voltage drop is measured instead of longitudinal.

Chapter 3

Results

3.1 Pure bismuth films

The results for the pure bismuth films are plotted in the order of increasing film thickness. The color coding for annealed and non annealed samples are the same for the whole section, so that black and red are films grown on SiO_x, black being the sample measured before annealing and red after annealing. Similarly for samples grown on mica, blue and green, respectively. Unfortunately, due to the difficulties of detaching the electrical contacts from the samples, measurement of the same sample before and after the annealing was not possible. Removing the indium caused the contact pads to break loose, and significant amount of indium was left in the vicinity of the samples. During the annealing it would have melted and contaminated the sample.

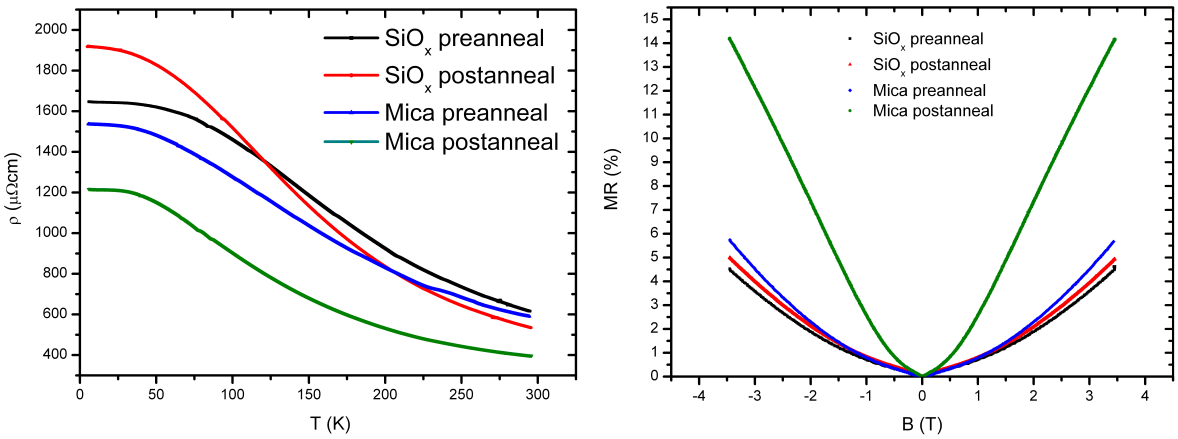

Figure 3.1: Resistivity and magnetoresistance of 65 nm thick bismuth films.

The resistivities and magnetoresistance for 65 nm films are plotted in figure 3.1. The magnetoresistance MR(%) is defined as

$$MR(\%) = \frac{R(B) - R(0)}{R(B)} \times 100\%. \tag{3.1}$$

The resistivity increases with decreasing temperature, whereas in bulk bismuth it decreases. The non-metallic resistivity behavior may be due to the small grain size of around 100 – 200 nm (fig. 3.7) in these films. The small grain size leads to significant grain boundary scattering. This scattering mechanism is almost independent of temperature. The increase in resistivity is thus due to decreasing carrier concentration. In bulk bismuth, the carrier concentration decreases ten-fold from 300 K to 4.2 K, but the mobilities increase 3.5 orders of magnitude [33], which have more strongly opposing effect on the resistivity.

For the 65 nm films the annealing decreases the overall resistivity, and lower resistivity is found on the samples grown on mica. The effect of annealing to resistivity is quite peculiar, since in many samples a significantly higher resistivity is found after annealing at low temperatures. The room temperature resistivity is usually lower. The magnetoresistance increases only slightly after annealing in the sample grown on SiO_x, but a clear increase is found on the mica sample. The magnitude of the effect is still quite small.

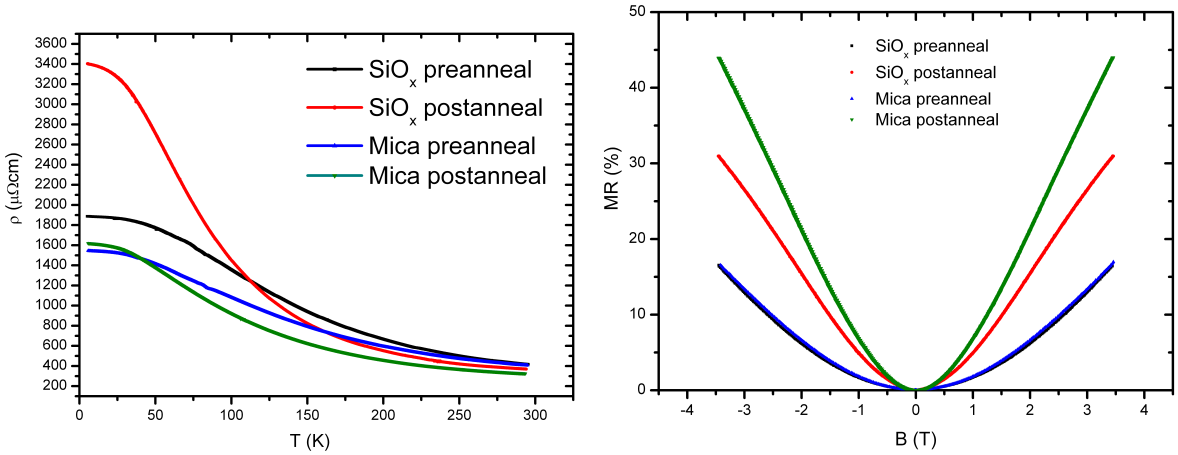

Figure 3.2: Resistivity and magnetoresistance of 125 nm thick bismuth films.

Results for 125 nm films are plotted in figure 3.2. For both substrates, the room temperature resistivity decreases by about 30 % after annealing, but at the low temperatures it increases, especially on the sample grown on SiO_x. The improvements on magnetoresistance are clear. The field dependence is quasilinear. The magnitude of the MR increases due to the increase in film thickness.

Similar plot for 380 nm films is presented in figure 3.3. The decrease in room temperature resistivity is significant, and the value $\sim$ 215 μΩcm is about twice the resistivity of bulk bismuth (107 μΩcm [32]). The low temperature resistivity of the sample grown on SiO_x increases. Upon post-annealing the magnetoresistance increases about 2.5 times for both samples in 3.5 T field, the sample grown on mica having larger value. The MR starts to show hints of high field saturation after annealing.

As a final addition, 1 μm thick films grown on SiO_x were measured. Results are

plotted in figure 3.5. Because of the increased thickness, the annealing produces some interesting results. The non annealed sample has similar properties as the thinner films, but the resistivity of the annealed film initially decreases with temperature, and starts to increase after $\sim$ 170 K. The measured room temperature resistivity $\sim$ 87 µΩcm is actually lower than the bulk resistivity, the error is probably due to the fact that the actual thickness is not 1 µm. It has been observed before that evaporated bismuth films with several micrometer thickness can have drastically different thickness compared to the thickness indicated by the quartz crystal microbalance [5]. The thickness of some of the thinner films were determined with AFM measurements and consistent results were found, but when the film thickness increases the polycrystalline structure can cause significant variations in the thickness. Also the leftover PMGI resist in the vicinity of the films made AFM imaging difficult or impossible for some of the samples. The overall resistivity of the annealed sample is signifigantly lower than that for the non annealed sample, even though there is some error in the actual values. Both the samples were evaporated in the same batch, so that they should have the same thickness.

The changes in the magnetoresistance for the 1 µm thick film after annealing are largest of all the samples, nearly ten-fold increase in the MR ratio at 3.5 T. The large MR of the annealed film caused problems in the Hall measurement (figure 3.6). Since the change in longitudinal resistivity was large and it was coupled to the longitudinal resistivity (misalignment of the Hall voltage tabs), the Hall resistivity was positive for *both* positive and negative magnetic fields. The Hall resistivity was non-symmetrical for high fields, which was due to the actual Hall effect. Due to these problems in the Hall measurement, the numerical analysis could not be applied to this sample.

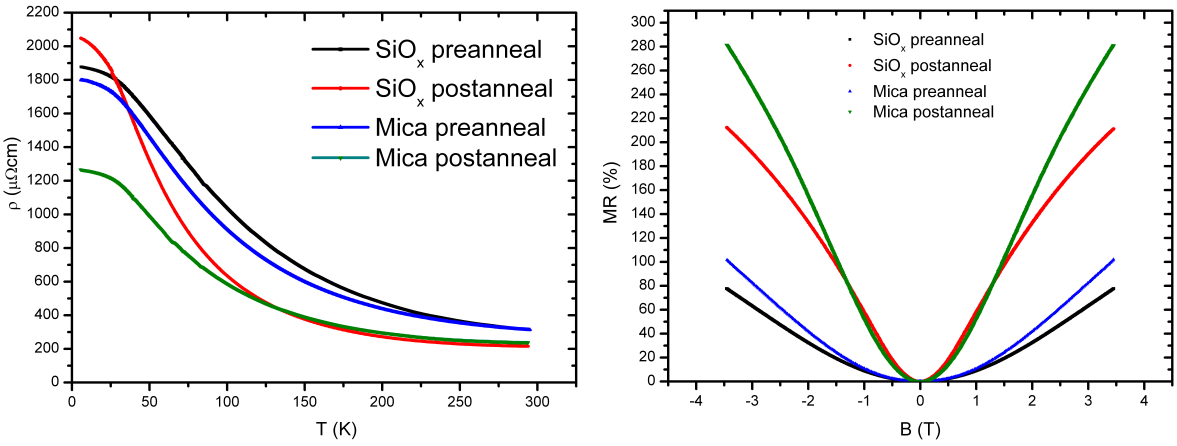

Figure 3.3: Resistivity and magnetoresistance of 380 nm thick bismuth films.

The results for Hall measurements are plotted in figure 3.4. The hall resistivity is calculated as $\rho_H = (V_H/I)t$, where I is the bias current and t is the thickness of the sample. The hall resistivity is negative, indicating that electronic conductance dominates in these films. The Hall resistivities are generally not linear in magnetic

fields. This is consistent with the theory. The behavior of hall resistivities roughly follow the behavior predicted by (1.38), so that the low field slope differs from the high field slope. Also the hall coefficient seems to increase after annealing.

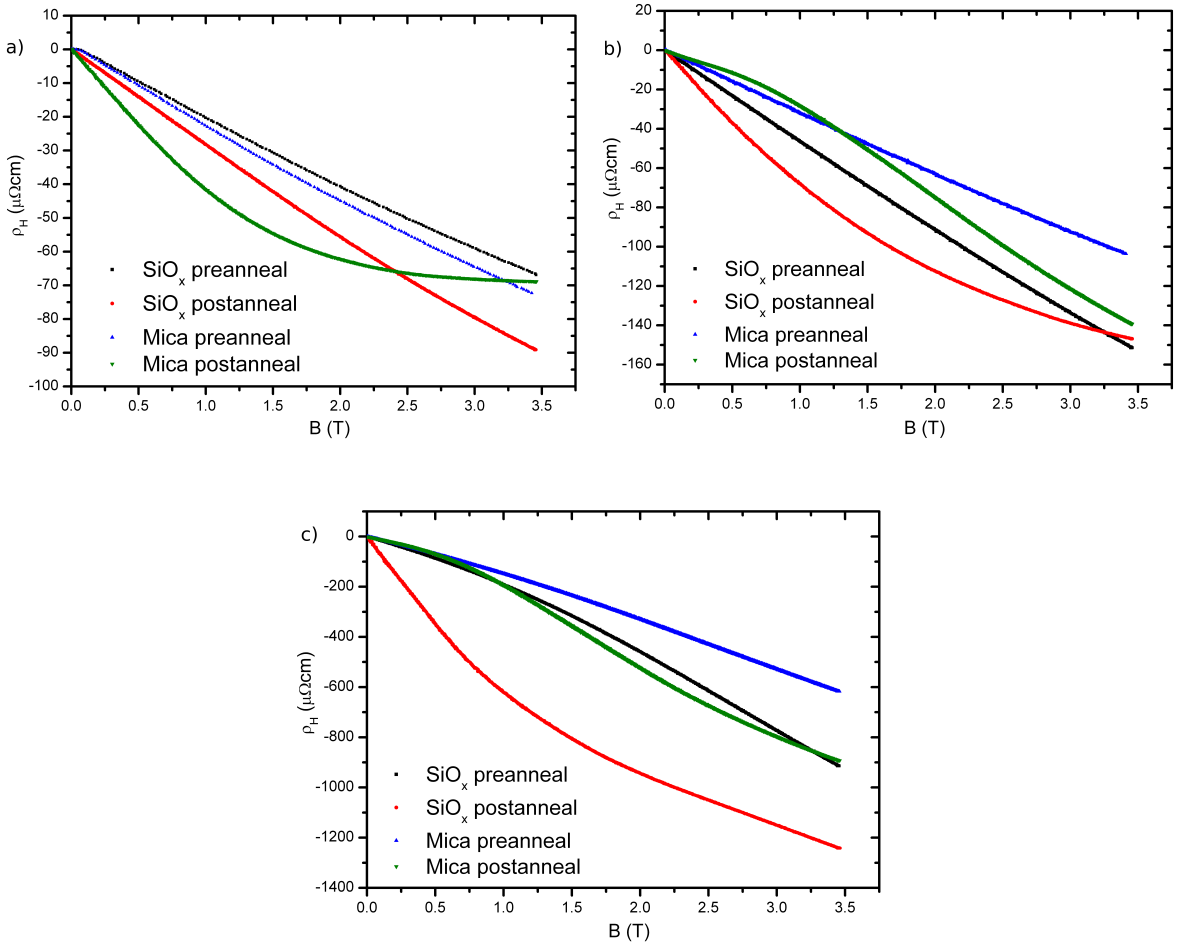

Figure 3.4: Hall resistivities for a) 65 nm, b) 125 nm, and c) 380 nm thick bismuth films.

SEM images of 125 nm films grown on SIO_x before and after the annealing are shown on figure 3.7. No significant change in the grain size is observed, and the same result was confirmed for samples grown on mica via AFM mesurements. The surface roughness of the films is large, the height of the whiskers are comparable to the "bulk" thickness of the film.

Figure 3.8 shows the results of the 2-wire resistance measurement during annealing for a 380 nm film on SiO_x. Since the electrical contacts to the sample were mechanical, in many cases the signal got lost at some point. Initially the resistance decreases with temperature, and a minimum is found around 150 ℃. When the annealing temperature is reached, the resistance starts slowly decreasing, and drops signifigantly when the sample is cooled down. The 8 hour annealing seemed sufficient, since further annealing of same sample for 6 hours did not cause further change in the room temperature

resistance. The room temperature resistance dropped typically about 40 %.

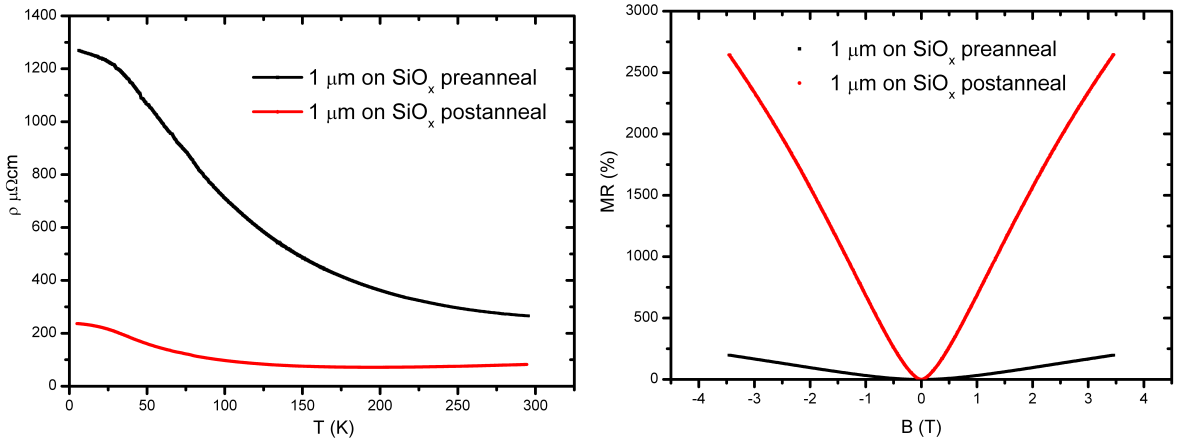

Figure 3.5: Resistivity and magnetoresistance of 1 µm thick bismuth films grown on SiO_x.

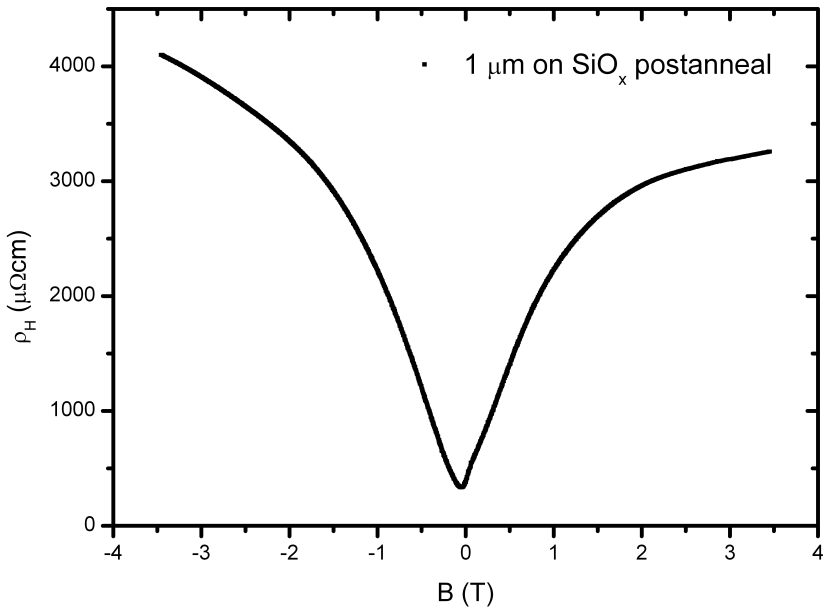

Figure 3.6: Hall resistivity for 1 µm thick annealed bismuth film grown on SiO_x. The Hall resistivity is positive for both orientations of the magnetic field, because of the strong magnetoresistance effect and its coupling to the Hall resistivity (misalignment of the Hall voltage tabs).

Table 3.1: The resistivities of the samples at 295 K and 4.2 K.

Sample	ρ (295 K) (µΩcm)	ρ (4.2 K) (µΩcm)
65 nm (SiO) preanneal	618	1649
65 nm (SiO) postanneal	535	1920
65 nm (Mica) preanneal	590	1536
65 nm (Mica) postanneal	397	1216
125 nm (SiO) preanneal	417	1887
125 nm (SiO) postanneal	369	3403
125 nm (Mica) preanneal	406	1544
125 nm (Mica) postanneal	325	1619
380 nm (SiO) preanneal	315	1877
380 nm (SiO) postanneal	215	2047
380 nm (Mica) preanneal	313	1799
380 nm (Mica) postanneal	238	1266
1 µm (SiO) preanneal	266	1270
1 µm (SiO) postanneal	83	237
3/122 nm Au/Bi preanneal	614	1730
3/122 nm Au/Bi postanneal	250	3104
2/63 nm Au/Bi preanneal	694	1548
2/63 nm Au/Bi postanneal	695	1978
Bulk	107	

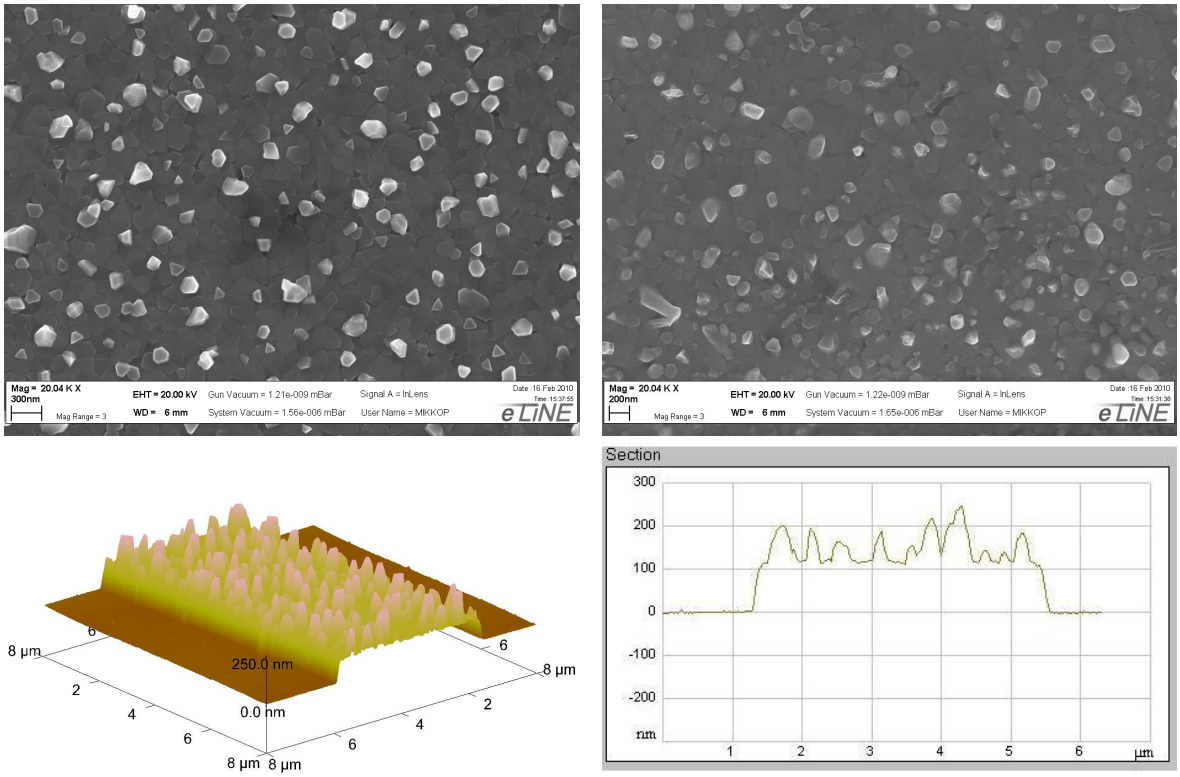

Figure 3.7: SEM images of 125 bismuth films grown on SiO_x, before (left) and after annealing (right). The AFM image (bottom) shows the surface roughness of an as deposited 125 nm film. The height of the whiskers is comparable to the "bulk" thickness of the film, as can be seen from the line scan on the bottom right.

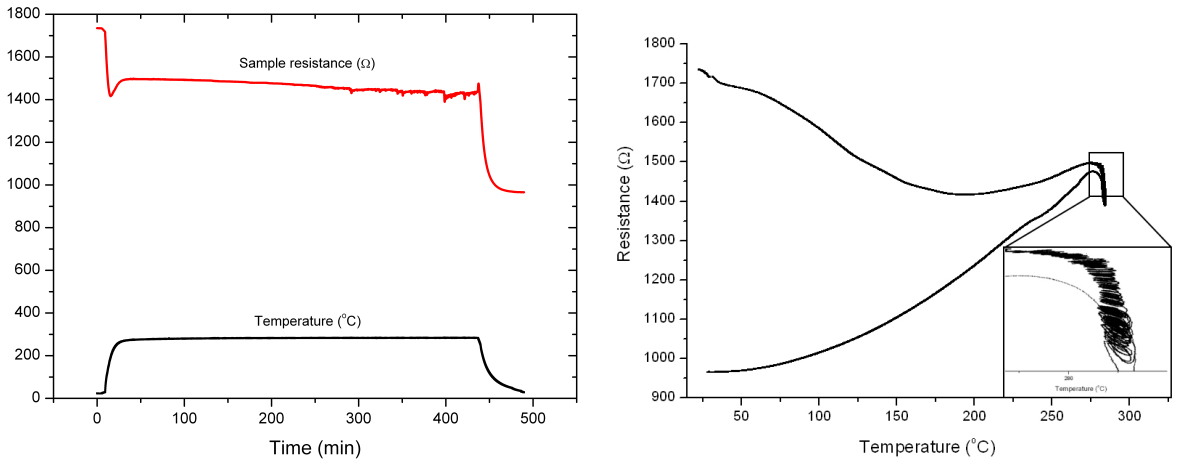

Figure 3.8: An example of the 2-wire resistance measurement for a 380 nm film grown in SiO_x. Left: temperature and resistance as a function of time. Right: Resistance vs temperature of the same sample, the upper curve shows the resistance behavior during warming up, and the lower curve is taken when cooling down.

3.2 Au-Bi films

The resistivities and magnetoresistance of gold/bismuth films grown on SiO_x are plotted in figure 3.9. The low temperature resistivity increases for both samples, especially for the 125 nm film. The room temperature resistivity of this sample is quite low, but the temperature dependence is strongly non metallic. The magnetoresistance is quite high already before annealing compared to the samples without the gold layer, and after annealing the MR is slightly higher than in the pure films.

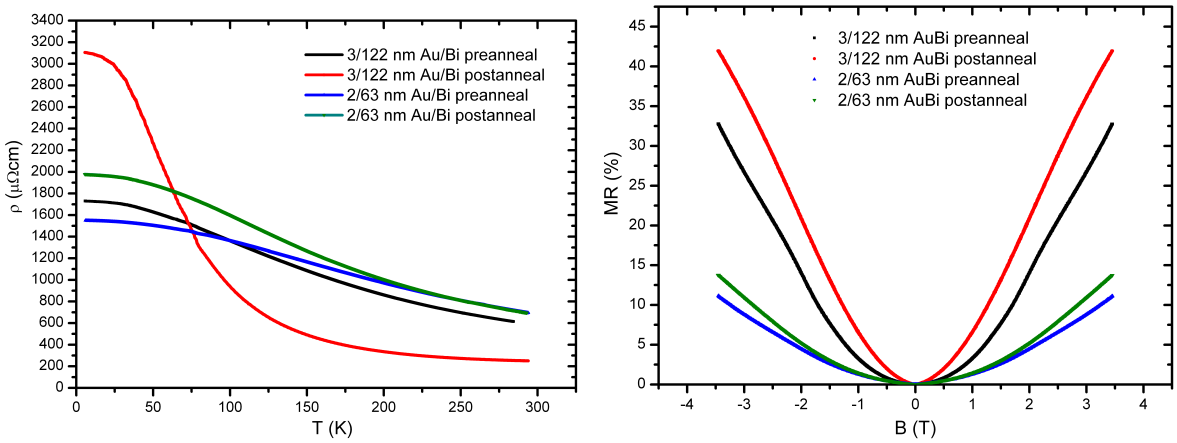

Figure 3.9: Resistivities and magnetoresistance of gold/bismuth films grown on SiO_x.

3.3 Extraction of carrier mobilities and concentrations

In order to extract the carrier mobilities and concentrations from the magnetotransport data, the slope of the low field Hall voltage has to be evaluated. For example, for the case of annealed 380 nm film grown on mica, the Hall voltage is roughly linear up to 0.4 T. The fit is shown in figure 3.10. The factor A from eq. (1.41) can be calculated with the known zero field conductivity. The non linear two parameter fits to (1.44) were done with Wolfram Mathematica software. Note that here the magnetoresistance ratio is defined as $r = R(B)/R(0)$, instead of as in eq. (3.1). The fit for the annealed 380 nm film on mica with the fitting parameters are shown in figure 3.11.

The fitting results seem to be good, and the 95 % confidence intervals for the estimated parameters μ_e and μ_h are tight. This indicates the model fits the data well. A fitting procedure used by the authors of [34], where they fitted the magnetoresistance ratio of a 342 nm film grown on mica to the expression (1.36), with μ_e, μ_h, and c as free parameters. They gave $\pm$ 50 % error range for their parameter estimates, indicating that the fit was not very reliable. When similar fitting was done on data presented here, the numerical algorithm did not converge to an unambiguous minimum. In the

two parameter model the errors in the fit are smaller than 1 %, showing clearly the effectiveness of our method.

The carrier concetration ratio c was calculated with the obtained parameters from (1.42), and the electron concentration with (1.39) or (1.40). There was deviation of few percent in the electron density calculated from these two expressions. There is also uncertainty in the low field Hall voltage slope and in the zero field conductivity, so that the total error in the final parameters are estimated to be around 10 %. The results for all the samples are presented in Table 3.2.

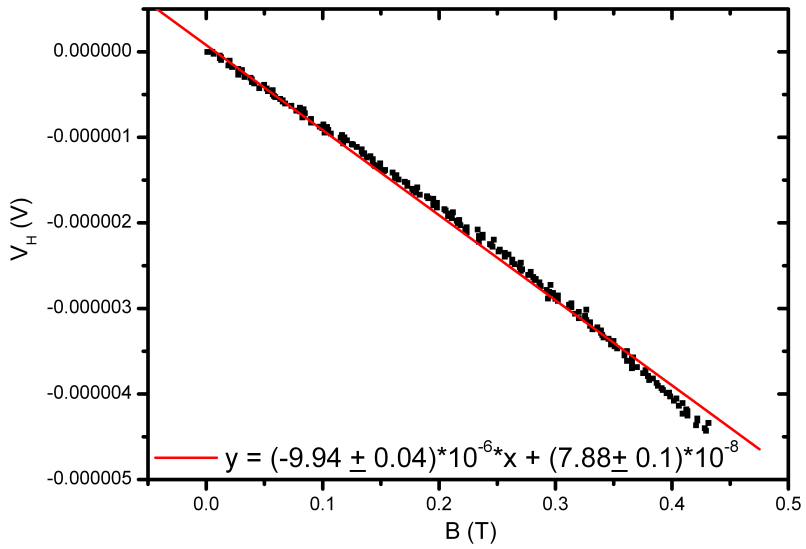

Figure 3.10: Low field Hall voltage for annealed 360 nm film grown on mica.

There are some interesting findings in the fitting results. Overall the mobilities are quite small compared to the bulk, and they increase with film thickness and with annealing. Electrons seem to outnumber holes in all samples, especially in the thinner ones. Their mobilities are somewhat smaller than hole mobilities, in contrast to the situation in bulk bismuth. The electron majority is in agreement with [34]. As for the electron density, it is more than 10 times higher in the 65 nm films than the electron density in bulk bismuth. This could be due to the surface states whose relative contribution is greater in the thinner films [19]. The electron density seems to decrease after annealing in all cases, and for the 380 nm films it is close to bulk density.

Table 3.2: Carrier mobilities and concentrations extracted from the transport data at 4.2 K. Parameter uncertainties are around ± 10 %

Sample	μ_e (m^2/Vs)	μ_h (m^2/Vs)	c=p/n	n ($1/cm^3$)
65 nm (SiO) preanneal	0.04	0.22	0.02	$8.2 \cdot 10^{18}$
65 nm (SiO) postanneal	0.04	0.25	0.01	$7.9 \cdot 10^{18}$
65 nm (Mica) preanneal	0.05	0.22	0.03	$1.0 \cdot 10^{19}$
65 nm (Mica) postanneal	0.01	0.38	0.04	$4.5 \cdot 10^{18}$
125 nm (SiO) preanneal	0.1	0.20	0.17	$3.1 \cdot 10^{18}$
125 nm (SiO) postanneal	0.14	0.41	0.09	$1.0 \cdot 10^{18}$
125 nm (Mica) preanneal	0.09	0.23	0.12	$3.4 \cdot 10^{18}$
125 nm (Mica) postanneal	0.17	0.43	0.14	$1.6 \cdot 10^{18}$
380 nm (SiO) preanneal	0.29	0.38	0.32	$8.1 \cdot 10^{17}$
380 nm (SiO) postanneal	0.84	0.99	0.32	$2.6 \cdot 10^{17}$
380 nm (Mica) preanneal	0.32	0.41	0.39	$7.2 \cdot 10^{17}$
380 nm (Mica) postanneal	0.67	0.92	0.41	$4.6 \cdot 10^{17}$
1 µm (SiO) preanneal	0.60	0.64	0.38	$5.8 \cdot 10^{17}$
3/122 nm Au/Bi preanneal	0.23	0.29	0.18	$1.3 \cdot 10^{18}$
3/122 nm Au/Bi postanneal	0.18	0.43	0.13	$8.4 \cdot 10^{17}$
2/63 nm Au/Bi preanneal	0.11	0.21	0.08	$3.2 \cdot 10^{18}$
2/63 nm Au/Bi postanneal	0.11	0.19	0.13	$2.3 \cdot 10^{18}$
Bulk	38.0 - 68.0	2.1 - 12.0	1.04	$2.88 \cdot 10^{17}$

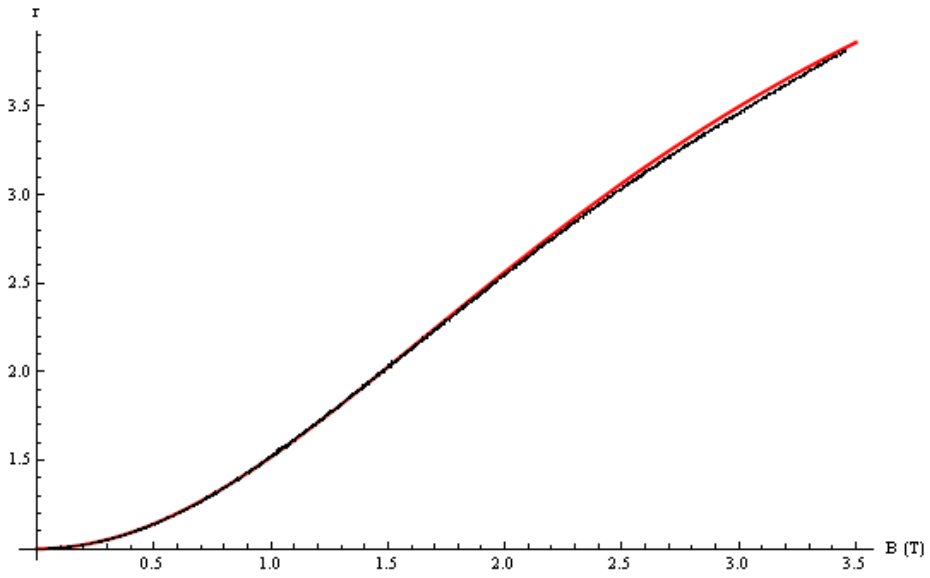

{BestFitParameters → {a → 0.666673, b → 0.918468},

ParameterCITable →

	Estimate	Asymptotic SE	CI
a	0.666673	0.0000788922	{0.666518, 0.666828},
b	0.918468	0.000196272	{0.918083, 0.918853}

EstimatedVariance → 0.0000502098,

ANOVATable →

		DF	SumOfSq	MeanSq
Model		2	20077.9	10039.
Error		3341	0.167751	0.0000502098,
Uncorrected Total		3343	20078.1	
Corrected Total		3342	2886.55	

AsymptoticCorrelationMatrix → $\begin{pmatrix} 1. & 0.975207 \\ 0.975207 & 1. \end{pmatrix}$,

FitCurvatureTable →

	Curvature
Max Intrinsic	0.000268541
Max Parameter-Effects	0.000936697
95. % Confidence Region	0.577502

}

Figure 3.11: The non linear fit to the magnetoresistance data for annealed 380 nm film grown on mica. The resulting fit parameters are presented below, with a = μ_e and b = μ_h. The CI interval is a 95 % confidence interval for the estimated parameter values.

Chapter 4

Conclusions

In summary, it seems that the annealing used in this work increases the magnetoresistance in all the samples studied, but the resistivity behavior is still non-metallic and the mean grain size does not grow significantly in these films. This is in contrast to previous studies with thicker, over 1 µm thick films, where the grain size increased after annealing the sputtered films deposited on SiO_x [31]. The magnetoresistance at 3.5 T of our annealed 125 nm pure bismuth film grown on mica is roughly the same as an as deposited 300 nm film grown on SiO_x in Ref [35]. Also, the annealed 380 nm films show higher magnetoresistance than electrodeposited, non annealed 10 µm films [36]. The magnitude reported here, $\sim$ 250 % is comparable to GMR at low temperatures [37].

The observation of increased resistivity in many samples at low temperatures versus consistent increase in magnetoresistance is intriguing. The SEM images showed that the grain size does not change in films grown on SiO_x, and the same result was confirmed with AFM measurements for the films grown on Mica. The increased magnetoresistance implies that some scattering mechanism is decreased, which was not reflected in the resistivity. The basic two carrier model cannot explain this properly, since the classical magnetoresistance ratio depends on (for a compensated metal) $r \sim 1 + \mu_e\mu_h B^2 = 1 + (\tau_e/m_e^*)(\tau_h/m_h^*)e^2B^2$. Increase in magnetoresistance implies increase in τ or equivalently in the mean free path, which would happen due to the grain size growth and should be reflected in the resistivity. Thus some other scattering mechanism is suppressed after annealing.

In these experiments the gold underlayer in the samples deposited on SiO_x improved the magnetoresistance slightly compared to the pure films, but the other electrical properties remained mostly unaffected. The large magnetoresistance observed before annealing is probably due to the rearrangement of the film during evaporation, so that the gold diffuses into the film during deposition and alters the grain formation.

The results from the 1 µm thick film support the idea that the annealing improves the properties of the "bulk" part of the film, so that the thicker the film, the more is the effect of annealing on its properties. The surface roughness does not change or at least it does not decrease, and its contribution to the film properties is larger in thinner

films.

The analysis method combining the information from Hall measurements and magnetoresistance seemed successful at least in terms of fitting accuracy. The estimates obtained for mobilities and carrier concentrations are more reliable than in previous studies [34], and the values are also in agreement with previous results.

Bibliography

[1] N. Garcia, Y.H. Kao, M. Strongin, *Galvanomagnetic studies of bismuth films in the quantum-size-effect region*, Phys. Rev. B **5**, (1972)

[2] D. H. Reneker, *New oscillatory absorption of ultrasonic waves in bismuth in a magnetic field*, Phys. Rev. Lett. **1**, 440 (1958)

[3] A. Boukai, K. Xu, J.R. Heath, *Size-dependent transport and thermoelectric properties of individual polycrystalline bismuth nanowires*, Adv. Mater. **18**, 864-869, (2006)

[4] S. Jin, M. McCormack, T.H. Tiefel, R.Ramesh, *Colossal magnetoresistance in La-Ca-Mn-O ferromagnetic thin films*, J. Appl. Phys. **76** (10), (1994)

[5] M. Palosaari, *Transition edge sensor array development*, Master's thesis, University of Jyväskylä, Department of Physics, Nanoscience Center, (2009)

[6] Xu Du, *Magnetotransport and tunneling study of the semimetals bismuth and graphite*, PhD. thesis, University of Florida, 2004

[7] Stephen B. Cronin, *Electronic properties of Bi nanowires*, PhD. thesis, Massachusetts Institute of Technology, 2002

[8] Lax B., Mavroides J.G, in *Solid State Physics*, vol. 11, page 261, Academic Press, New York, 1960

[9] Kittel, C., 1996, *Introduction to solid state physics*, 7th edn, Wiley: New York

[10] Dresselhaus M.S., Lin Y.-M., Cronin S.B., Rabin O., Black M.R., Dresselhaus G., *Quantum wells and quantum wires for potential thermoelectric applications*, Semimetals and Semiconductors **71**, Academic Press, 2001

[11] Vecchi, M.P., Dresselhaus M.S., Phys. Rev. B **10**, 771 (1974)

[12] Pippard, A.B., *Magnetoresistance in Metals*, Cambridge University Press, 1989

[13] Alers, P.B., Webber, R.T., *The magnetoresistance of bismuth crystals at low temperatures*, Phys.Rev. **91**, 1060 (1953)

[14] Madou M.J., *Fundamentals of microfabrication: The science of miniaturization*, 2nd Edition, CRC Press, USA, (2002)

[15] Brodie, I and Muray, J.J., *The physics of micro/nanofabrication* Plenum Press, New York, (1992)

[16] P.Rai. Choulduri, *Handbook of microlithography, micromachining and microfabrication, vol 1: Microlithography*, Electronics & Communication Engineering Journal **10**, (1998)

[17] Partin D.L., Heremans D.T., Morelli C.M., Olk C.M., Perry T.A., *Growth and characterization of epitaxial bismuth films*, Phys. Rev. B. **38**, (1988)

[18] Sunglae Cho, Yunki Kim, L.J. Olafsen, I. Vurgaftman, A.J. Freeman, G.K.L. Wong, J.R. Meyer C.A. Hoffmann, J.B. Ketterson, *Large magnetoresistance in post-annealed polycrystallinen and epitaxial Bi thin films*, Journal of Magnetism and Magnetic Materials **239**, 201–203, (2002)

[19] Mei LU, R.J. Zieve, A. van Hulst, H.M. Jaeger, T.F. Rosenbaum, *Low-temperature electrical-transport properties of single-crystal bismuth films under pressure*, Phys Rev. B **53**, number 3, (1996)

[20] F.Y. Yang, Kai Liu, C.L. Chien, P.C. Searson, *Large magnetoresistance and finite-size effects in electrodeposited single-crystal bi thin films*, Phys. Rev. Lett. **82**, number 16, (1999)

[21] F.Y. Yang, Kai Liu, Kimin Hong, D. H. Reich, P.C. Searson, C.L. Chien, Y. Leprince-Wang, Kui Yu-Zhang, *Shubnikov–de Haas oscillations in electrodeposited single-crystal bismuth films*, Phys. Rev. B **10**, number 10, (2000)

[22] C.L. Chien, F.Y. Yang, Kai Liu, D.H. Reich, *Very large magnetoresistance in electrodeposited single-crystal Bi thin films*, Journal of Applied Physics **87**, number 9, (2000)

[23] Xu Du, A.F. Hebard, *Large magnetoresistance of bismuth/gold films thermally deposited onto glass substrates*, Applied Physics Letters **82**, number 14, (2003)

[24] K.A. Padmanabhan, M.D.C Moles, G.J. Davies, *Orientation of bismuth films on mica*, Journal of Materials Science **12**, (1977)

[25] H.T. Chu, P.N. Henriksen, J. Alexander, *Resistivity and transverse magnetoresistance in ultrathin films of pure bismuth*, Phys. Rev. B **37**, number 8, (1988)

[26] H.T. Chu, P.N. Henriksen, Jing Jing, Hong Wang, Xiaofeng Xu, *Magnetic-field dependence of Hall resistance in thin films of pure bismuth*, Phys. Rev. B **45**, number 19, (1992)

[27] M.E. Fleet, R.A. Howie, *Rock forming minerals: Mica rock forming minerals vol 3a*, 2nd edition, Geological Society Publishing House, (2004)

[28] http://www.britannica.com/EBchecked/topic/379747/mica#, viewed 05/2010

[29] http://www.microchem.com/products/pdf/PMGI-Resists-data-sheetV-rhcedit-102206.pdf, viewed 05/2010

[30] E. Zoro., E. Dichi, C. Servant, B. Legendre, *Phase equilibria in the Ag-Au-Bi ternary system*, Journal of Alloys and Compounds **400**, 209-215, (2005)

[31] Joonyeon Chang, Hijung Kim, Junhyun Han, M.H. Jeon, W.Y. Lee, *Microstructure and magnetoresistance of sputtered bismuth thin films upon annealing*, Journal of Applied Physics **98**, 023906, (2005)

[32] Generalic, Eni. "Bismuth." *EniG. Periodic Table of the Elements*, 27 Feb. 2010. KTF-Split. http://www.periodni.com/en/bi.html Viewed 05/2010.

[33] J. Heremans, C.M. Thrush, Yu-Ming Lin, S. Cronin, Z. Zhang, M.S. Dresselhaus, J.F. Mansfield, *Bismuth nanowire arrays: Synthesis and galvanomagnetic properties*, Phys Rev. B **61**, 2921, (2000)

[34] Ralph Rosenbaum, Jean Galibert, *Unusual electronic transport properties of a thin polycrystalline bismuth film*, Journal of Physics: Condensed Matter **16**, 5849-5867, (2004)

[35] N. Marcano, S. Sangiao, J.M. De Teresa, L. Morellon, M.R. Ibarra, M. Plaza, L. Perez, *Structural and magnetotransport properties of Bi thin films grown by thermal evaporation*, Journal of Magnetism and Magnetic Materials **322**, 1460-1463, (2010)

[36] B. O'Brien, M. Plaza, L.Y. Zhu, L. Perez, C. L. Chien, P. C. Searson, *Magnetotransport properties of electrodeposited bismuth films*, J. Phys. Chem. C **112**, 12018-12023, (2008)

[37] E.E. Fullerton, M.J. Conover, J.E. Mattson, C.H. Sowers, S.D. Bader, *150 % magnetoresistance in sputtered Fe/Cr(100) superlattices*, Appl. Phys. Lett. **63**, 1699, (1993)